MOLECULAR DYNAMICS MODELLING OF GOLD ATOMIC FORCE MICROSCOPY TIPS ON MULTILAYER GRAPHENE

A THESIS SUBMITTED TO
THE GRADUATE SCHOOL OF NATURAL AND APPLIED SCIENCES
OF
MIDDLE EAST TECHNICAL UNIVERSITY

BY

CEM MADEN

IN PARTIAL FULFILLMENT OF THE REQUIREMENTS
FOR
THE DEGREE OF MASTER OF SCIENCE
IN
PHYSICS

SEPTEMBER 2020

Approval of the thesis:

MOLECULAR DYNAMICS MODELLING OF GOLD ATOMIC FORCE MICROSCOPY TIPS ON MULTILAYER GRAPHENE

submitted by **CEM MADEN** in partial fulfillment of the requirements for the degree of **Master of Science in Physics Department, Middle East Technical University** by,

Prof. Dr. Halil Kalıpçılar
Dean, Graduate School of **Natural and Applied Sciences** _____

Prof. Dr. Altuğ Özpineci
Head of Department, **Physics** _____

Assoc. Prof. Dr. Hande Toffoli
Supervisor, **Physics, METU** _____

Examining Committee Members:

Assoc. Prof. Dr. Engin Durgun
Institute of Material Science and Nanotechnology, Bilkent Uni. _____

Assoc. Prof. Dr. Hande Toffoli
Physics, METU _____

Assist. Prof. Dr. Osman Barış Malcıoğlu
Physics, METU _____

Date: _____

I hereby declare that all information in this document has been obtained and presented in accordance with academic rules and ethical conduct. I also declare that, as required by these rules and conduct, I have fully cited and referenced all material and results that are not original to this work.

Name, Surname: Cem Maden

Signature :

ABSTRACT

MOLECULAR DYNAMICS MODELLING OF GOLD ATOMIC FORCE MICROSCOPY TIPS ON MULTILAYER GRAPHENE

Maden, Cem
M.S., Department of Physics
Supervisor: Assoc. Prof. Dr. Hande Toffoli

September 2020, 56 pages

Simultaneously with the developing industry, nanotribological properties of nanoscale materials, especially in the fields of friction and lubrication, have been the subject of growing research. Interactions between materials are usually analyzed with modified atomic force microscopy (AFM) devices using lateral force measurement and topographic imaging techniques. Thanks to its superior physical and chemical properties, graphene has remained influential in the industry, including its use as a lubricant. Direct simulations of realistic interactions between AFM tips and graphene are, however, rarely performed in literature. In this thesis, nanotribological properties between graphene and gold AFM tips have been examined using molecular dynamics simulation. The AFM tip was modeled in various possible geometries and the graphene substrate as a slab with multiple layers during the investigation. The AFM tip's lateral forces on the substrate were analyzed in detail as a function of several parameters, including tip velocity, temperature, vertical load, and tip size.

Keywords: Molecular Dynamics, Friction, Graphene, AFM simulation

ÖZ

ÇOK KATMANLI GRAFEN ÜZERİNDE ALTIN ATOMİK KUVVET MİKROSKOP UÇLARININ MOLEKÜLER DİNAMİĞİ MODELLEMESİ

Maden, Cem
Yüksek Lisans, Fizik Bölümü
Tez Yöneticisi: Doç. Dr. Hande Toffoli

Eylül 2020 , 56 sayfa

Gelişen endüstri ile eş zamanlı olarak, nano ölçekli malzemelerin nanotribolojik özellikleri, özellikle sürtünme ve kayganlaştırma alanlarında, gelişen araştırmaların konusu olmuştur. Malzemeler arasındaki etkileşimler genellikle yanal kuvvet ölçümü ve topografik görüntüleme teknikleri kullanılarak modifiye edilmiş atomik kuvvet mikroskobu (AFM) cihazlarıyla analiz edilir. Üstün fiziksel ve kimyasal özellikleri sayesinde grafen, kayganlaştırıcı olarak kullanımı da dahil olmak üzere endüstride önemini korumuştur. AFM uçları ve grafen arasındaki gerçekçi etkileşimlerin doğrudan simülasyonları, literatürde nadiren yapılmaktadır. Bu tezde grafen ve altın AFM uçları arasındaki nanotribolojik özellikler moleküler dinamik simülasyonu kullanılarak incelenmiştir. İnceleme sırasında, AFM ucu çeşitli olası geometrilerde ve grafen yüzeyi birden çok tabakalı bir levha olarak modellendi. Yüzey üzerindeki AFM ucunun yanal kuvvetleri, uç hızı, sıcaklık, dikey yük ve uç boyutu dahil olmak üzere çeşitli parametrelerin bir fonksiyonu ayrıntılı olarak analiz edildi.

Anahtar Kelimeler: Moleküler Dinamik, Sürtünme, Grafen, AKM simulasyonu

To my familiy

ACKNOWLEDGMENTS

I am grateful to Assoc. Prof. Hande Toffoli for her support at every stage, with guidance, patience and encouragement. I am very happy to have the opportunity to have her mentoring.

I would like to thank fellow the Computational Material Science Group members Gözdenur Toroman, Gizem Özcan, Ümit Doğan Dağlum and Fırat Yalçın, Elif Sert for their suggestions, supports and great friendships.

This work is financially supported by TÜBİTAK (The Science and Technological Research Council of Turkey). (Grant no:115F493)

Last but most certainly not least, I sincerely thank my family for their support.

This accomplishment would not have been possible without them and I would like to thank them deeply.

TABLE OF CONTENTS

LIST OF TABLES

TABLES

LIST OF FIGURES

FIGURES

LIST OF ABBREVIATIONS

ABBREVIATIONS	
2D	2 Dimensional
AFM	Atomic Force Microscopy
MLG	Multilayer Graphene
MD	Molecular Dynamics
LJ	Lennard Jones
EAM	Embedded Atom Model
LAMMPS	Large-scale Atomic/Molecular Massively Parallel Simulator
AIREBOD	Adaptive Reactive Intermolecular Bond Order Potential
REBO	Reactive Bond Order
DFT	Density Functional Theory
FCC	Face Centered Cubic
fs	Femtosecond
nN	Nanonewton
Uni	Universite
MSD	Mean Square Displacement

CHAPTER 1

INTRODUCTION

Mechanical systems and machines contain many materials in their structures that interact with each other. The friction, lubrication, and wear properties of the materials play a significant role in the efficiency and the lifetime of these machines. The study of these principles is called tribology, which is first discussed in 1996 [3]. Tribological studies have shown us that energy losses due to friction are not negligible. In fact, the energy required to overcome friction is about the 20% of total energy use in the industry [4]. As a result, a significant amount of attention must be paid in order to reduce this excessive amount of energy loss.

Studies conducted in the material science to reduce the energy loss caused by friction are based on Atomic Force Microscopy (AFM), by acquiring nanotribological information from the material such as lateral forces, surface potential, stiffness, stress, etc. Besides this, predictions and understanding the behavior of materials using computational material science simulations have reduced the cost and increased the speed of researches [5].

1.1 Graphene

Graphene is a single layer of the honeycomb lattice structure, which is sp2-hybridized carbon atoms arranged in 2D [6]. It has great properties such as being strong, flexible, thin, transparent and being have high electrical and thermal conductivity. Due to the extraordinary mechanical properties, graphene, graphite, and carbon nanotube are used as reinforcements in various fields [7] [8].

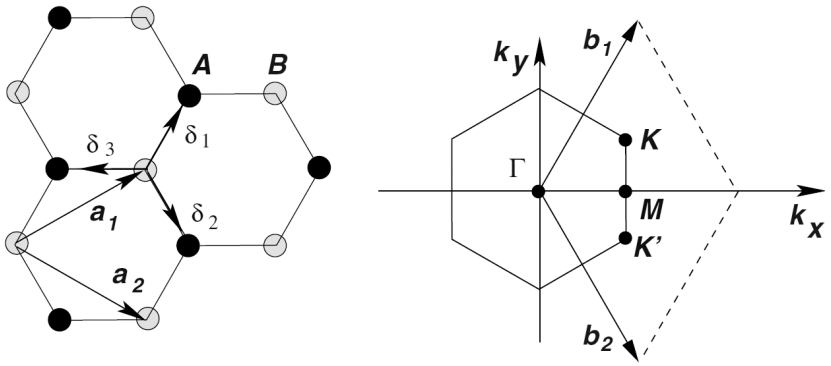

Figure 1.1: Lattice structure and reciprocal lattice of graphene taken from [1].

$$\vec{\delta_1} = \frac{a}{2}(1, \sqrt{3}) \qquad \vec{\delta_2} = \frac{a}{2}(1, -\sqrt{3}) \qquad \vec{\delta_3} = -a(1, 0) \tag{1.1}$$

$$\vec{a_1} = \frac{a}{2}(3, \sqrt{3}) \qquad \vec{a_2} = \frac{a}{2}(3, -\sqrt{3}) \tag{1.2}$$

$$\vec{a_i}.\vec{b_j} = 2\pi\delta_{ij} \qquad \vec{b_1} = \frac{2\pi}{3a}(1, \sqrt{3}) \qquad \vec{b_2} = \frac{2\pi}{3a}(1, -\sqrt{3}) \tag{1.3}$$

Where, a is the molecular bond length of graphene ($\approx$ 1.42 Å), $\vec{a_1}$ and $\vec{a_2}$ are lattice vectors, $\vec{b_1}$ and $\vec{b_2}$ are reciprocal lattice vectors, $\vec{\delta_1}$, $\vec{\delta_2}$ and $\vec{\delta_3}$ are nearest-neighbor vectors in real space.

Young's modulus of single layer graphene, which has 0.335 nm effective thickness, is 1.0 ± 0.1 TPa [9]. On the other hand, the strength of graphene is nearly 130 GPa, which means it is a very flexible substance as well as strong [9]. Since the interaction between graphene layers is weak van der Waal's forces, the vertical strength of multilayer graphene is not high as the horizontal strength.

1.2 Atomic Force Microscopy

In a general way, AFM is created by coated with the desired material of the sharp end of the console connected to a mechanism that can be moved at the desired speed. The

holder of the console can measure the force caused by interactions with the surface, and the mechanism can follow the angular movements of the console by sending a diode laser beam onto the console and absorbing the reflected beam.

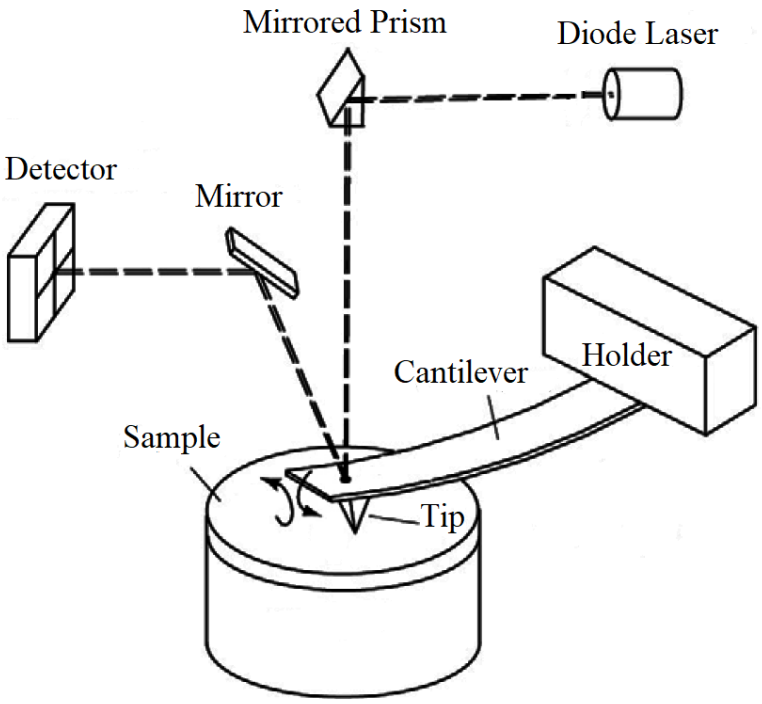

Figure 1.2: Schematic representation of the AFM mechanism modified from [2].

Using the measurement of force, topographic imaging, and manipulation techniques, AFM allows to obtain mechanical properties and high resolution surface images of substances and directly affect the sample. There are contact, non-contact, and tapping modes that will be used to study friction, viscosity, stiffness, topographical properties. The mechanism where lateral force tests are performed can be called as Friction Force Microscopy that can be categorized as a static mode, such as the contact mode. The friction between the contact mode AFM tip and the surface creates tension on the surface as a consequence stick-slip movement is expected while friction tests are carried out [2]. The structure of the AFM tip may experience a degradation effect that will cause differences in experiments that will take place after [10]. The hardness of the material on which the AFM tip is coated can prevent structural deterioration, but the coating material can affect the flexibility and force constant of the console.

1.3 Friction Between Gold and Graphene

Materials apply each other force while sliding against each other. This force is resistance to motion and is called friction. At the atomic level, the friction force is explained by the Tomlinson model (1929) [11], which is still used today. Tomlinson models the friction phenomenon as the drag of a nanotip over a corrugated surface by a spring [12]. Due to the spring and corrugated surface, the nanotip continues its movement by jumping; it performs the stick-slip [13] phenomenon. Based on this model, spring constant as the stiffness of a material, sliding direction [14], contact area [15], and temperature [16] will significantly impact friction.

Gold is a widely chosen material as a probe coating in direct contact AFM applications [17]. On the other hand, graphene is one of the preferred materials as a lubricant [18]. Studies involving gold and graphene are available in the literature. The distribution of gold nanoparticles on graphene [19], the drag force between the gold nanocrystal and graphene [20], the graphene creation on gold [21] are among the topics previously researched. The friction between these two materials is also a critical tribology study. Friction was investigated by sliding the gold flake on graphene, changing the gold structure and rotation angle and vertical load [22]. There has been a lack of proper studies for empirical experimental conditions to better examine the friction between these two materials.

The arrangement of the carbon atoms in the graphene structure and the fact that the bond direction between the carbon atoms can be clearly selected will help us to examine the effect of the slip direction on friction. We aimed to study the contact surface by creating the gold AFM type in different ways. Considering the spring constant in the Tomlinson model as the flexibility of the probe, in some simulations, it is simulated as rigid. At this point, the reason we do not use a substance with higher stiffness is that it is not possible to make a comparison because its interaction with graphene will be different from gold.

1.4 Overview

In this thesis, the nanoscale friction force between the gold AFM tip and 4 layer graphene is analyzed by using MD theory. The simulations were organized into 2 parts to examine the effect of temperature and shape difference and for the hemisphere shape of tip size and unfixed structure. Au(1,1,1) atoms are positioned in the shape of the pyramid, hemisphere and cone and 4 layer armchair graphene created as AB stacking as a surface of a substrate. After the tip and graphene are brought to the desired temperature, they are brought to the desired distance by bringing them closer to each other from a long distance. The tip is slid in different distances and temperatures in x and y directions. The speed of the AFM tip is $10\ \frac{cm}{s}$ during all runs. The experiments were repeated at lower and higher speeds before speed selection was made. Higher speeds prevented stick-slip movement, while lower speeds increased computational time significantly. considering the properties of the system to be simulated, the most appropriate speed has been decided as $10\ \frac{cm}{s}$.

CHAPTER 2

MOLECULAR DYNAMICS

2.1 Introduction

Molecular dynamics is a technique for simulating many-particle systems at the atomic scale based on Classical Mechanics. MD simulations solve Newton's equation of motion for many-particle systems, representing the interparticle interactions by suitable empirical models. The accuracy of the MD simulations, therefore, largely depends upon the accuracy of these empirical models. The interatomic potentials are usually created as models with a fair number of adjustable parameters, each of which can be fitted to either available experimental data or results from more accurate theoretical calculations. The effect of electrons is taken into account only explicitly, and therefore, the interaction emerges as a function only of the atomic position. As a result, the force on the i_{th} atom needed for Newton's equation of motion is written as a simple gradient of the interaction energy concerning its position. Potentials can be created by using experimental values directly or theoretical functions.

$$\vec{F_i} = -\nabla_i U(\vec{r}_1, \vec{r}_2, \vec{r}_3, ..., \vec{r}_N) \tag{2.1}$$

where $\vec{r_i}$ is the position of i^{th} atom. Since the system has force information,

$$\vec{F_i} = m_i \frac{d^2\vec{r_i}}{dt^2} \tag{2.2}$$

can be written by using Newton's 2^{nd} law of motion.

Once the position-dependent forces, initial positions, and initial velocities are known,

the solution of the system of equations of motion for all atoms is a matter of integrating forward in time using a suitable algorithm. There are a large number of such algorithms, and the suitable ones must be chosen such that conservation of energy and the stability of the algorithm are ensured.

In this thesis, the investigation of the nanotribalogical properties of Graphene and Gold interfaces is aimed. To perform this investigation, open-source software Large-scale Atomic/Molecular Massively Parallel Simulator (LAMMPS) [23] is used for the integration of MD calculations.

2.2 Molecular Dynamics Algorithms

Many algorithms for the time-integration needed to solve equations of motion are based on Taylor's expansion. Some important examples to these algorithms are Verlet [24], velocity-Verlet [25], Leap-Frog and Beeman's [26] algorithm. Integration schemes should be time-reversible, which is an important property of any realistic simulations. Otherwise, the second law of thermodynamics would have been neglected [27]. Verlet and velocity-Verlet algorithm are well known and most commonly used algorithms due to their performance and relatively small errors in terms of the discrete time step.

2.2.1 Verlet Algorithm

The Verlet algorithm is based on finite differences. The atomic positions as a series in time can be obtained by combining the time backward and forward Taylor series expansion of position equations in time.

The forward and backward expansions are given respectively by;

$$\vec{r}(t+\Delta t) = \vec{r}(t) + \dot{\vec{r}}(t)\Delta t + \frac{1}{2!}\ddot{\vec{r}}(t)\Delta t^2 + \frac{1}{3!}\dddot{\vec{r}}(t)\Delta t^3 + \mathcal{O}(\Delta t^4) \qquad (2.3)$$

and

$$\vec{r}(t-\Delta t) = \vec{r}(t) - \dot{\vec{r}}(t)\Delta t + \frac{1}{2!}\ddot{\vec{r}}(t)\Delta t^2 - \frac{1}{3!}\dddot{\vec{r}}(t)\Delta t^3 + \mathcal{O}(\Delta t^4) \tag{2.4}$$

By adding Eq. (2.3) and Eq. (2.4) yields;

$$\vec{r}(t+\Delta t) + \vec{r}(t-\Delta t) = 2\vec{r}(t) + 2\frac{1}{2!}\ddot{\vec{r}}(t)\Delta t^2 + \mathcal{O}(\Delta t^4) \tag{2.5}$$

and rearranging Eq. (2.2) leas to the Verlet algorithm;

$$\vec{r}(t+\Delta t) = -\vec{r}(t-\Delta t) + 2\vec{r}(t) + \frac{F(t)}{m}\Delta t^2 + \mathcal{O}(\Delta t^4). \tag{2.6}$$

The Verlet algorithm produces new positions using those obtained in the previous two time steps and forces while an error of order Δt^4. Although the Verlet algorithm is useful and straightforward, it has no built-in velocity terms. The calculation of velocities, which is necessary for determining the temperature and calculating relevant averages, must be done separately, which increases the computational cost. A similar method, the velocity-Verlet algorithm, has been developed to fix this shortcoming.

2.2.2 Velocity-Verlet Algorithm

Like Verlet, velocity-Verlet also combination of Eq. (2.3) and Eq. (2.4). The algorithm aims to include the velocity term to the Verlet method.

$$\vec{r}(t+\Delta t) = \vec{r}(t) + \dot{\vec{r}}\Delta t + \frac{\vec{a}(t)}{2}\Delta t^2 \tag{2.7}$$

$$\vec{v}(t+\Delta t) = \vec{v}(t) + \frac{\vec{a}(t) + \vec{a}(t+\Delta t)}{2} + \Delta t \tag{2.8}$$

It can rigorously be proven that the error in the velocity-Verlet integration scheme is identical to that generated in the ordinary Verlet scheme. Simultaneously, the four-step integration algorithm discussed below ensures that the computational load and the memory demand remains the same as well.

Calculating positions at new timestep;

$$\vec{r}(t+\Delta t) = \vec{r}(t) + \dot{\vec{r}}\Delta t + \frac{\vec{a}(t)}{2}\Delta t^2 \tag{2.9}$$

Calculating velocity at half timestep;

$$\vec{v}(t+\frac{1}{2}\Delta t) = \vec{v}(t) + \frac{\vec{a}(t)}{2}\Delta t \tag{2.10}$$

Using new positions Eq. (2.9) and potential, calculating the new acceleration;

$$\vec{a}(t+\Delta t) = -\frac{1}{m}\nabla\vec{V}(\vec{r}_{1\ldots N}) \tag{2.11}$$

Finally the new velocity is

$$\vec{v}(t+\Delta t) = \vec{v}(t) + \frac{\vec{a}(t)+\vec{a}(t+\Delta t)}{2}\Delta t \tag{2.12}$$

2.3 Interatomic Potentials

Potentials and mass information of atoms are keys for turning out numerical positions to significant atomic particles in simulations. As mentioned previously, once a suitable model represents the interaction potential between the atoms, MD simulations can quickly be conducted by integrating Newton's equations of motion.

$$\vec{F_i} = -m_i\frac{\partial U}{\partial \vec{r_i}} \qquad m_i\ddot{\vec{r}_i} = -\vec{F_i} \tag{2.13}$$

where $\vec{F_i}$, $\vec{r_i}$ and U represents the force on atom i, position of atom i and potential respectively.

As stated earlier, once a system containing potentials is created with a suitable model, MD simulations can efficiently reassign atomic positions using specific algorithms. Unlike *ab initio* calculations, the choice of the interatomic system is system-dependent. The type of bonds between the atoms should be taken into account while this choice

is made. For example, using the Embedded Atom Model (EAM) [28], which is designed for metals for systems with directional bonds, will result in substantial errors. It may even be possible to obtain different lattice constants for the same system using two different interatomic potentials.

In its most general form an N-particle intertomic potential can be written as;

$$U(\vec{r}_1, \vec{r}_2, \vec{r}_3, ..., \vec{r}_N) = \sum_i U_1(\vec{r}_i) + \sum_i \sum_{j>i} U_2(\vec{r}_i, \vec{r}_j) + \\ + \sum_i \sum_{j>i} \sum_{k>j} U_3(\vec{r}_i, \vec{r}_j, \vec{r}_k) + ... \tag{2.14}$$

where $\vec{r}_i$ is the position of the ith atom. The first single-body term usually represents external fields; the second is a pairwise interaction, while the third describes angle-dependent terms. This is an infinite series in principle. However, in most applications, it is truncated in the third term.

In the systems investigated in this thesis, non-bonded interactions are the most important component of the interaction, determining all the relevant physical quantities of interest. Therefore, it is important to work with potentials that describe such interactions reasonably well. Pair potentials are often used for describing non-bonded interaction between two particles of the same or different species. These potentials are usually parameterized to reproduce the experimental bond lengths and bond distances. Lennard-Jones potential [29] and Morse potential [30] are well known pair potentials.

Many-body potentials are used for describing the interaction between three or more particles. It may include the angle between particles/molecules and electron density around the particle according to the system type.

Lennard-Jones potential, Embedded Atom Model, and AIREBO potential [31] as many-body potentials are discussed in next sections.

2.3.1 Lennard-Jones Potential

Lennard-Jonnes potential [29] is simple function that can describe Van der Waals attraction [32] and the Pauli-Repulsion [33] in high accuracy. Therefore, potential contains both attractive and repulsive terms;

$$U_{LJ}(r) = 4\epsilon \left[\left(\frac{\sigma}{r}\right)^{12} - \left(\frac{\sigma}{r}\right)^{6} \right] \tag{2.15}$$

where σ is the distance between particle when the inter-potential of two particles is zero and ϵ is the potential energy when it reaches the minima.

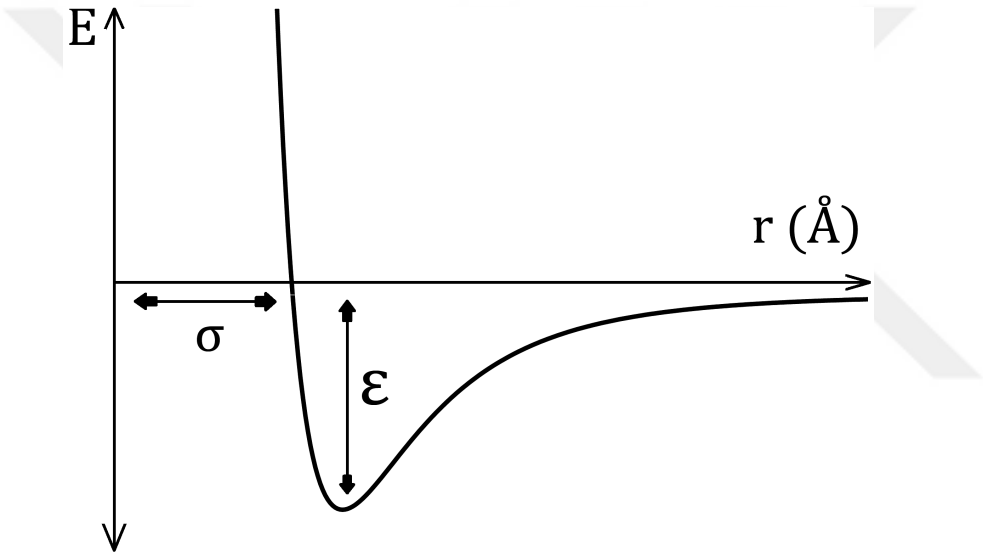

Figure 2.1: Schematic of the Lennard-Jones 6-12 Potential.

In principle, the Lennard-Jones interaction between every pair in the simulation box should be calculated. However, we only include pairs within a certain cut-off distance to reduce the computational cost to a manageable amount in practice. The value of cut-off distance should be adjusted depending on how rapidly the interaction decays. Choosing too low and high cut-off distances can affect the reliability of potential.

$$U_{LJ} = \begin{cases} 4\epsilon \left[\left(\frac{\sigma}{r}\right)^{12} - \left(\frac{\sigma}{r}\right)^{6} \right] & r \leq r_c \\ 0 \quad r > r_c \end{cases} \tag{2.16}$$

In this thesis, Lennard-Jones potential is used to describe interaction between Gold and Carbon atoms. r_c chosen as 15 Å. Whereas σ and ϵ constants are 3.003 Å and $0.0341\ eV$ respectively which are taken from [34].

```
## Usage of Lennard Jones potential in LAMMPS
pair_style lj/cut cutoff
pair_coeff type1 type2 lj/cut ϵ σ
# cutoff: cutoff for Lennard Jones interactions
# type1 and type2: groups of atoms to interact
# ϵ and σ: Lennard Jones parameters
```

2.3.2 Embedded Atom Model

The embedded atom model (EAM) [28] refers to an interatomic interaction potential parametrized specifically for metallic systems. In this study, we used EAM potential to describe interactions between Gold atoms. The main idea is calculating the total energy of a system by using a summation of pair interaction and energy, which is needed to position an atom within the electronic background density. EAM is given by [35] as;

$$E_{total} = \sum_{i=1}^{N} \left[E_i(\bar{\rho}_i) + \frac{1}{2} \sum_{j=i}^{N} U_{pair}(r_i j) \right] \tag{2.17}$$

where U_{pair} is the pair potential and $E_i(\bar{\rho}_i)$ is the energy against the background electron density $\bar{\rho}_i$ to move an atom from infinity to the desired location. The background energy density is average electron densities of atoms.

```
## Usage of EAM potential in LAMMPS
pair_style eam
pair_coeff type1 type2 ../potentials/file.eam
# type1 and type2: groups of atoms to interact
# file.eam: name of the potential file
```

2.3.3 Adaptive Reactive Intermolecular Bond Order Potential(AIREBO)

In this thesis, we use the Adaptive Reactive Intermolecular Bond Order Potential (AIREBO) [31] to describe is used for expressing atomic interactions between Carbon atoms. Like EAM, Airebo also includes terms besides pair interaction. To represent covalent bonding between atoms, Airebo uses the Reactive Bond Order (REBO) [36] method with additional Lennard Jonnes and torsion terms;

$$E_{ij} = E_{ij}^{Rebo} + E_{ij}^{LJ} + \sum_{k \neq i,j} \sum_{l \neq i,j,k} E_{ij}^{Torsion} \tag{2.18}$$

where E^{Rebo} and E^{LJ} are the energies associated with bond order and Lennard-Jones method respectively. $E^{Torsion}$ is the energy describing torsion about covalent bonds.

$$E_{ij}^{Rebo} = E_{ij}^{Repolsive}(r_{ij}) + b_{ij} E_{ij}^{Attractive}(r_{ij}) \tag{2.19}$$

where b_{ij} term describes strength of the covalent bonding due to chemical effects.

```
## Usage of AIREBO potential in LAMMPS
pair_style airebo cutoff
pair_coeff * * ../potentials/CH.airebo C C
# cutoff: cutoff for Lennard Jones interactions term
```

2.4 Thermodynamic Ensembles In MD

An MD simulation aims to calculate experimentally accessible, i.e., average quantities for a system. Therefore an appropriate thermodynamic ensemble should be used. Different types of ensembles can be used for the system, depending on the environment we are trying to simulate.

2.4.1 Microcanonical Ensembles

In microcanonical ensembles, the total energy of the system remains the same. In fact, the system is not allowed to exchange particles, energy, and change volume or shape. In our calculations, we allow the system to evolve within an NVE ensemble in the beginning to reach thermal equilibrium. Due to the lack of temperature control [37], NVE ensembles can not behave like a real experiment if the system temperature is not equilibrium [38]. NVT and NPT ensembles are better for modeling experimental conditions [39].

2.4.2 Canonical Ensembles

Canonical ensembles [40] represent systems that are at thermal equilibrium with a heat bath. In the language of computational physics and chemistry, numerical tools representing heat baths are referred to as thermostats. Thermostats will be discussed after the ensembles section. During simulations, the temperature is calculated by using average kinetic energy;

$$T(t) = \frac{1}{k_b N_f} \sum_i m_i v_i^2(t) \tag{2.20}$$

where k_B is the Boltzmann constant and N_f is the number of degrees of freedom.

2.5 Thermostats

There are several algorithms to control the temperature in MD. One such algorithm is the Anderson thermostat [41]. The main idea behind Anderson's algorithm is performing stochastic collisions with fictitious particles. Therefore, the momentum of particles in the actual system changes suddenly without affecting other particles. From this point of view, the process becomes not realistic since velocity differences can be high. Unlike the Anderson thermostat, the Nose-Hoover thermostat is an algorithm that does not use stochastic collisions [42]. The Nose-Hoover algorithm is based on adding new fictitious variables to the Lagrangian while the Hamiltonian

is unchanged. However, the disadvantage of using this method is that the speed of energy transmission is slow. The Gaussian thermostat is also a non-stochastic thermostat, which can be classified as a velocity rescaling method. It is a simple algorithm to control the temperature. The main idea is rescaling velocity, considering the new temperature and instantaneous temperature of the system. In this method and similar others, the system's instantaneous temperature is periodically calculated using Eq. (2.20), and the velocities are rescaled to reach the target temperature. The simplest rescaling that can be used is

$$p_i \rightarrow \sqrt{\frac{T_o}{T}} P_i \tag{2.21}$$

where T and T_o are the targets and actual temperature of particles. Although it is a fast and straightforward method, the Gaussian thermostat can not simulate the realistic experiment since it does not allow temperature fluctuation. Furthermore, scaling velocity in each time step causes discontinuity of momentum. Some algorithms can control temperature without causing discontinuity of momentum. Langevin [43] and Berendsen [44] thermostats, which will be discussed in the next two sections, are two of them.

2.5.1 Langevin Thermostats

Langevin thermostat [43] is a stochastic thermostat where the existing system is allowed to exchange kinetic energy with a fictitious reservoir of small particles. These fictional small particles can be thought of as acting like a sea around the main system. Total force should include terms due to random collisions, pairwise interaction, and drag force arising from the sea analogy:

$$\vec{F} = \vec{F}^c + \vec{F}^d + \vec{F}^d \tag{2.22}$$

Where $\vec{F}^c$, $\vec{F}^d$ and $\vec{F}^d$ are the conservative force, drag term and force due to bumping. Random force can be calculated using the fluctuation-dissipation theorem.

```
## Usage of Langevin Thermostat in LAMMPS
fix ID group_ID langevin Tstart Tstop Tdamp seed
#  ID: user assigned name for the fix
#  group_ID: name of the group of atoms
#  Tstart: system temperature
#  Tstop: desired temperature
#  Tdamp: damping parameter of thermostat
#  seed: positive number to use for random generator
# while generating white noise
```

2.5.2 The Berendsen Thermostats

The Berendsen thermostat [44] is the improved version of the Gaussian thermostat. In comparison, the Gaussian method adjusts the temperature to the desired value directly, Berendsen thermostat couples the system to a heat bath. As a result, temperature fluctuations are allowed. The rate of change in the temperature at each time step is related to the coupling parameter τ;

$$\frac{dT}{dt} = \frac{T_0 - T}{\tau} \tag{2.23}$$

where T_0 and T is desired and instantaneous temperature, respectively. τ is the time it takes the system to reach the new temperature.

This method of resclaing amounts to a transfer in the momentum;

$$p_i \rightarrow \lambda p_i \tag{2.24}$$

where λ is scailing factor given by;

$$\lambda^2 = 1 + \frac{\Delta t}{\tau_T}\left(\frac{T_0}{T} - 1\right) \tag{2.25}$$

In our calculations, we choose to use the Berendsen thermostat due to its simplicity and the availability of the temperature fluctuations.

```
## Usage of Berendsen Thermostat in LAMMPS
fix ID group_ID temp/berendsen Tstart Tstop Tdamp
#  ID: user assigned name for the fix
#  group_ID: name of the group of atoms
#  Tstart: system temperature
#  Tstop: desired temperature
#  Tdamp: damping parameter of thermostat
```

2.6 Preparation of the System and Errors Encountered

In this section, practical aspects of the simulation and physical properties of the prepared system are mentioned. The protocols described in this section are the selection and definition of the main constants of the simulation, and also include the problems that can be encountered during simulation.

2.6.1 Determination of Time Step

One of the most crucial parameters of MD simulations is the time step chosen for the Verlet integrations. A correct choice of this time step must balance accuracy against efficiency. Choosing a time step that is too large results in unrealistically large displacements and the system's eventual collapse. On the other hand, choosing small time step results in prohibitively long simulations, and it does not give enough time to vibrate some phonons. The general practice in MD communities is to choose a time step that is just small enough to resolve the fastest atomic vibration modes [45]. In line with this principle, we choose a time step of 1 fs. This choice is also in agreement with most MD studies in literature [46] [47].

2.6.2 Creation of Position Files

To simulate an AFM tip, the shape of the gold system is chosen as a hemisphere. Atoms are placed in the Face-Centered-Cubic (FCC) order, which is the atomic structure of gold at room temperature. In the AFM aspect, Au(111) is an ideal choice because of its flat shape [48]. To prevent the stability of this flat hemisphere shape, some of the top layers are fixed in the simulation. Also, to analyze the shape differences in our study, pyramidal, conic, and hemispherical shapes are created as fixed objects as it is more challenging to maintain these molds' shape.

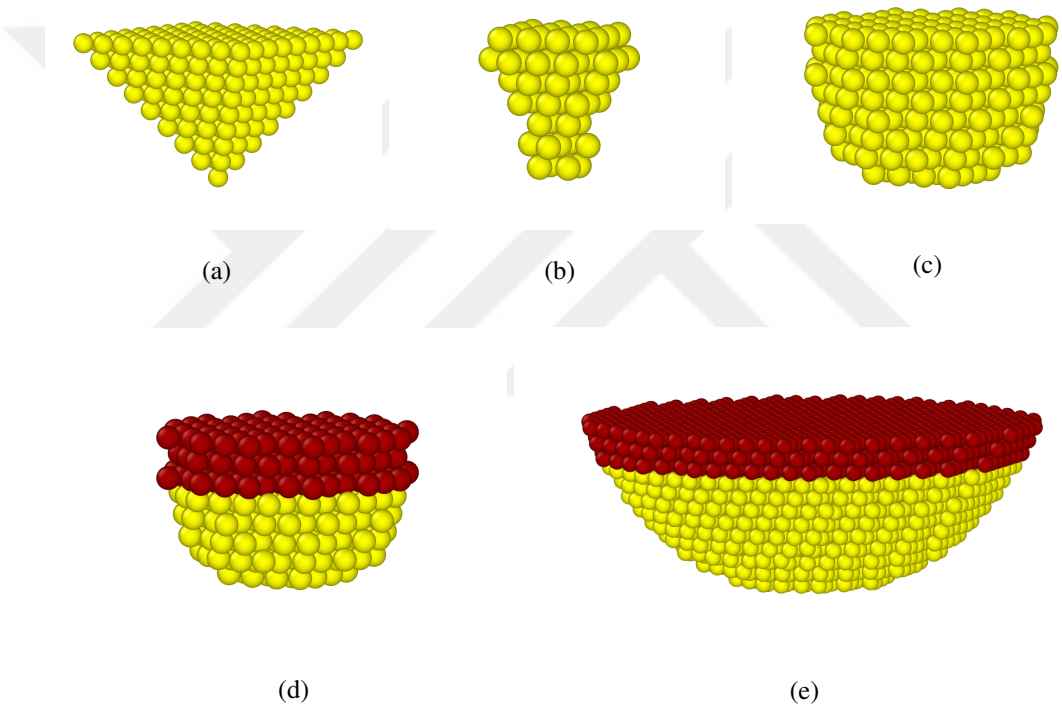

Figure 2.2: Different shapes of the gold tip. (a), (b) and (c) shapes are created with movement restrict gold atoms to prevent their pyramid, cone, and hemisphere shapes, respectively. (d), (e) shapes are created with two types of gold atoms. Red ones are movement restricted; yellow ones are mobile for these shapes. (c) and (d) has radius about 13 Å and (e) has radius about 30 Å but the bottom two layers were deleted to make the hemisphere look like an arc.

As shown in the Figure 2.2d and Figure 2.2e, the top layers of hemispherical gold AFM tips are fixed, which means that the force on these atoms are always zero. Care must be taken to exclude these atoms from calculations involving atomic coordinates, forces, or velocities. For example, those atoms were not included while measuring the force between gold and carbon atoms.

Four layers of Graphene were used to simulate the substrate. Due to the periodic boundary conditions used here, this substrate acts as an infinite surface. Similarly to the gold tip, the bottommost two layers of the graphene substrate are fixed during the simulations to prevent the layers from traveling large distances as the tip slides. This is a side effect of modeling a semi-infinite surface by using a finite slab.

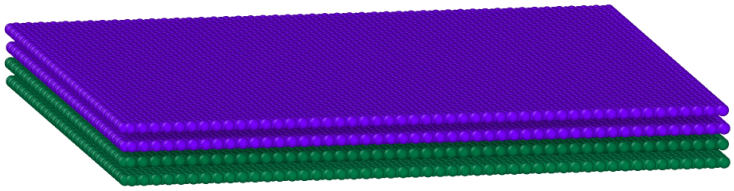

Figure 2.3: Four layered Graphene structure with fixed green atoms. Length in x and y directions are about 120 Å and 123 Å respectively. Area of the multilayer graphene is 14760 $Å^2$.

As the boundary conditions in the horizontal plane, the lengths of graphene were chosen to get periodicity. 100 $Å^2$ were determined as vertical boundary conditions. As these boundary conditions are sufficient for graphene to act as an infinite surface, the frequent interaction of the gold tip with itself is nearly zero.

2.6.3 Heating Process and Thermostat Choice

Heating and keeping simulation in the NVT ensemble are techniques to test simulation constants, atoms positions, potentials, etc. The system is heated and kept at different temperatures to avoid errors that may be encountered later. Although there are no two heat baths in the same place, tip and substrate are both heated individually and together. Langevin and Berendsen thermostats were also tested during this process. Berendsen is the chosen simulation thermostat. Although they give almost the same result at low temperatures, Graphene layers become unstable [49] (which was discussed in Section 2.6.6) at high temperatures while using Langevin thermostat.

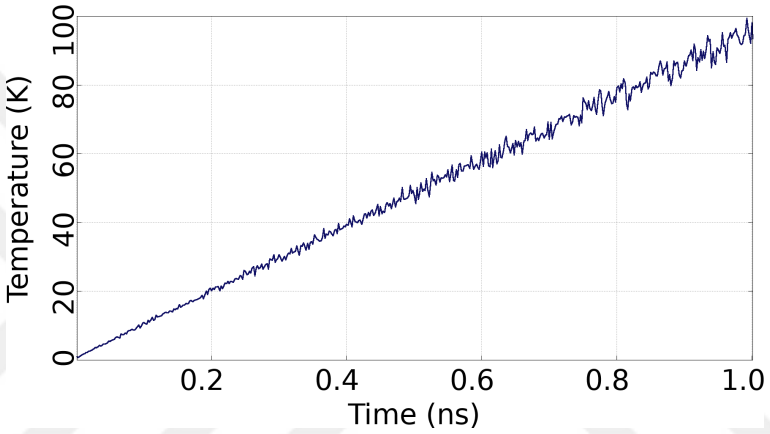

Figure 2.4: Temperature-Time graph of sample system heated from 0 to 100 Kelvin.

2.6.4 Final Preparations for Sliding Simulation

Before starting the sliding production runs, some more aspects of the system must be taken care of for a more realistic simulation. In real life, tip and substrate become closer just before the experiment. To simulate this event, tip and substrate are heated individually. And the tip is moved toward the substrate vertically at $10\ cm/s$ speed. While the tip is moving, restart files are created to be used later to initiate the sliding process. To prevent simultaneous energy and heat change, these systems waited in NVT ensemble for 1 ns simulation time before the sliding process.

2.6.5 Load Applying and Calculation Process

In a realistic experiment, the friction force is usually measured as a function of vertical load. However, in our calculations, as described in Section 2.6.2 the bottom two layers of the graphene material are fixed, as well as all or the top layers of the gold tip are fixed. Fixing the atoms on the golden tip prevents the vertical application of the load. This problem was solved by fixing the gold tip over the graphene substrate at certain distances. The value of the applied load was found using reverse engineering, that is, by calculating the force on the vertical axis after simulation. With this method, we are unable to conduct a calculation at a fixed load. However, the average load for a given vertical distance tends to remain the same throughout the sliding path. Therefore there is a near-one-to-one correspondence between distance and load. We present our results for fixed distances, which could also be interpreted, without a large error, to be fixed load calculations.

2.6.6 Independent Errors

While heating in process, horizontally shaking of graphene layers is observed in both Langevin and Berendsen thermostats. This problem is caused by the wrong calculation of equipartition of energy while velocity rescaling. In literature, this numerical error is called as flying ice cube [49]. The suggestion for the shaking layer problem is setting the linear momentum of layers manually. However, the manual intervention of the layers was not applied in order not to affect the results of calculations. This problem is solved by choosing Berendsen as the main thermostat, reducing the number of graphene layers, enlarging them in horizontal directions, and reducing the tip radius.

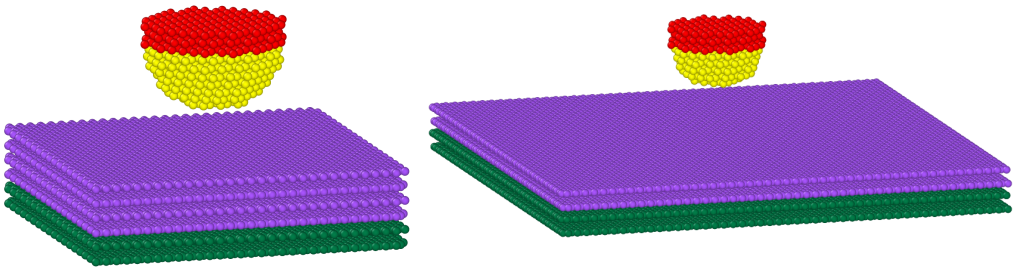

(a) (b)

Figure 2.5: Image of the old system with the changed one. (a) is the old system with 6 layered Graphene with hemisphere gold tip. (b) is the new one with 4 layered Graphene with smaller hemisphere gold tip.

Another critical issue is the choice of LJ parameters for non-bonded interactions since these interactions, for the large part, determine the tribological behavior. In literature, there are some rules to calculate parameters like Lorentz-Berthelot [50], Waldman-Hagler [51], Fender-Halsey [52] and Kong rules [53]. In the literature, the fact that there are too many rules to calculate the parameters has caused the parameters' variability. Parameters are taken from [34] due to the similarity of the systems used in the simulation and the research's reliability.

Fixing the Au atoms brings about the side effect where the Au tip's vertical load is no longer accessible. However, understanding the behavior of the system as a function of load is one of the most important aspects of this work. Therefore, we follow an implicit method where we calculate the lateral forces on the tip as a function of vertical distance and reverse-engineer the value of the load using interpolation. Details of this calculation will be presented in the relevant sections.

CHAPTER 3

INVESTIGATION OF RIGID TIPS AND GRAPHENE

In this section, we present results from a series of simulations where the atoms of the gold AFM tip are kept rigid while it slides. We utilize a Berendsen thermostat with a damping parameter of 1 fs and a velocity-Verlet algorithm for the integration. The details of both methods have been previously discussed.

3.1 Determination of Loads on Certain Distances

As discussed in Section 2.6.5, three different distances between the tips and graphene is selected to investigate the effect of the AFM tip under load. These distances are determined based on the distance between the top layer of graphene and the closest atom of the gold tip to this layer. These distances of 2 Å, 2.5 Å and 3 Å are named h_1, h_2 and h_3 respectively.

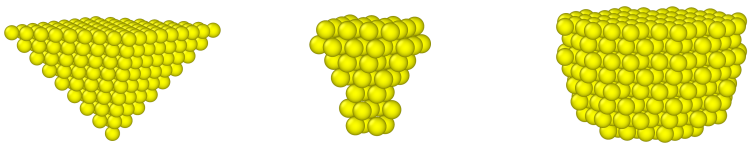

(a) (b) (c)

Figure 3.1: Rigid Gold AFM tips.

Loads are calculated by taking the average of the vertical component of the forces on all the tip atoms during the sliding process at room temperature. As expected from systems interacting via van der Waals forces, at large separations, the forces are attractive. As the vertical distance decreases, the forces become repulsive and the magnitude increases with decreasing distance because of the Pauli exclusion principle [54]. The magnitude of the forces increases with growing contact area between the graphene substrate and the tip.

Table 3.1: Average vertical force(nN) for different tips at different temperatures, loads and sliding directions. Where h_1, h_2 and h_3 are 2 Å, 2.5 Å and 3 Å respectively.

	Along	x	direction	Along	y	direction
	1K	100K	300K	1K	100K	300K
Pyramid						
h_1	2.521	2.636	2.829	2.525	2.643	2.833
h_2	0.264	0.348	0.510	0.282	0.362	0.515
h_3	-0.904	-0.856	-0.756	-0.878	-0.830	-0.723
Cone						
h_1	8.072	8.300	8.727	8.034	8.281	8.714
h_2	2.290	2.466	2.799	2.252	2.420	2.738
h_3	-0.782	-0.664	-0.401	-0.815	-0.688	-0.427
Hemisphere						
h_1	16.697	17.253	18.270	16.567	17.111	18.131
h_2	2.116	2.526	3.275	2.210	2.619	3.379
h_3	-4.010	-4.590	-4.886	-3.908	-4.496	-4.792

Keeping the tips at a constant distance made it feel more force in the vertical direction due to the increasing kinetic energy with the increase in temperature (see Table 3.1). The effect of varying vertical forces on friction force is examined in detail in the following sections.

Interestingly, lateral forces display a different behavior throughout the sliding process along the x and y directions, although the average forces are very close to each other. In order to highlight these different patterns, data gathered from simulations at 1K and h_3 distance are shown in Figure 3.2.

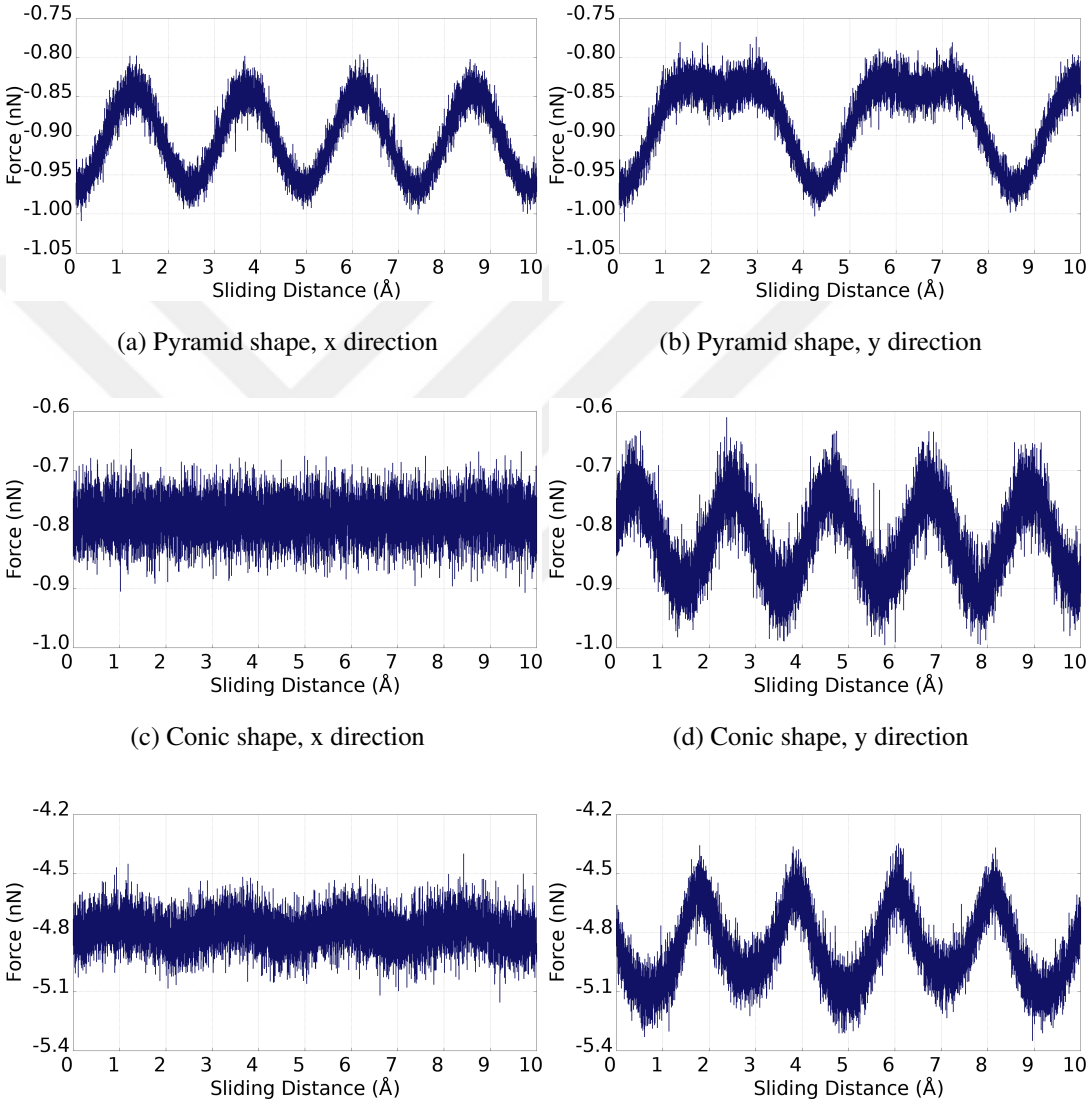

(a) Pyramid shape, x direction

(b) Pyramid shape, y direction

(c) Conic shape, x direction

(d) Conic shape, y direction

(e) Hemisphere shape, x direction

(f) Hemisphere shape, y direction

Figure 3.2: AFM tip sliding at 1K, speed $10\frac{cm}{s}$ and h_3 distance. The vertical component of the force with respect to distance.

The force profile as a function of sliding distance formed by sliding the conic and hemispherical tips along the x direction are flatter than the y direction. The reason for this is that along the y direction, the tips pass directly over C-C bonds, encountering the electron density in the bond perpendicularly. Furthermore, the contact surfaces of the tips are wider than the pyramid tip. Sliding the pyramid shaped tip in the x direction gives a zigzag shape in the Figure 3.2a by passing perpendicularly over the graphite bonds and contacting the surface by an atom at the end of the tip.

On the other hand, in the system sliding in the y direction, the pyramid tip passes directly over the bond in parallel to the bond resulting in the pattern shown in Figure 3.2b.

3.2 Analyzing Friction Force for Rigid Tips

In this section, the friction force will be analyzed using the force in a direction between gold and graphene obtained from simulation. These analyzes are created by shifting the tip of three different shapes at three different temperatures in two directions at a constant speed. In this way, it is aimed to examine the effect of temperature, sliding direction, load for a particular tip, and the effect of surface area on friction force for our system.

Temperatures are chosen as 1K to simulate absolute zero, 300K to simulate room temperature, and 100K to serve as an interpolating temperature inbetween. In addition to measuring different loads for each tip, the loads fluctuate during sliding. The basic idea behind choosing the tip shapes is that the shapes have different surface areas. The number of atoms around the contact surface is also important when considering the van der Waals interactions between gold and carbon atoms. The speed of the AFM tip is fixed in this section at $10\ \frac{cm}{s}$.

3.2.1 Friction Force for Pyramid Shape Tip

We start our investigation on the tip shape dependence of friction forces by considering a pyramidal tip. This is the sharpest tip studied in this section and served to

highlight the importance of sliding direction.

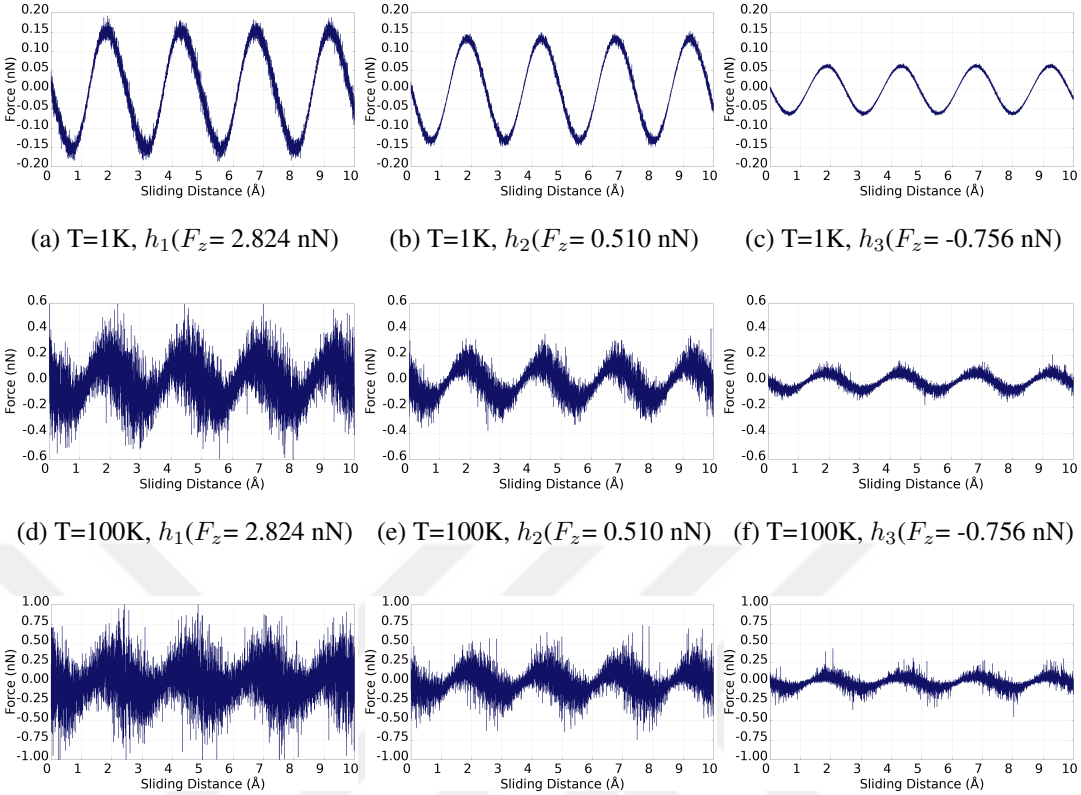

(a) T=1K, $h_1(F_z$= 2.824 nN) (b) T=1K, $h_2(F_z$= 0.510 nN) (c) T=1K, $h_3(F_z$= -0.756 nN)

(d) T=100K, $h_1(F_z$= 2.824 nN) (e) T=100K, $h_2(F_z$= 0.510 nN) (f) T=100K, $h_3(F_z$= -0.756 nN)

(g) T = 300K, $h_1(F_z$= 2.824 nN) (h) T = 300K, $h_2(F_z$= 0.510 nN) (i) T = 300K, $h_3(F_z$= -0.756 nN)

Figure 3.3: Pyramid shape tip sliding along x direction at speed 10 $\frac{cm}{s}$. X component of the force with respect to distance at different temperatures and loads.

As seen in the Figure 3.3, as the temperature(kinetic energy) is increased, the fluctuations of the data increase as expected from a system in an NVT ensemble. This effect is also seen in Figure 2.4, where the fluctuations in the temperature increase with increasing temperature. As the tip slides over and inbetween bonds and atoms, it samples hills and valleys of the potential energy surface. It is therefore expected to see a generalized periodic pattern.

In Figure 3.3, it is observed that the friction forces are increased with increasing temperature of the system since the increased temperature yields higher vertical force for our system (see Table 3.1) [55]. Likewise, it is obvious that the application of the loads in the vertical direction increases the friction force. There is more fluctuation

in the lower part of the graphs than in the upper part. The reason for this is that the accumulated elastic energy is transferred to phonon modes. Also, no stick-slip movement traces have been encountered since our tip shape is a rigid pyramid, which means the surface area is minimal. Although the friction test seems to be a single process, when examined in nanoscale, there is an adhesion process in addition to sliding between materials. Oscillation of the sliding phenomenon between surfaces is called stick-slip motion. There is no requirement for molecular bonding in this static friction phenomenon.

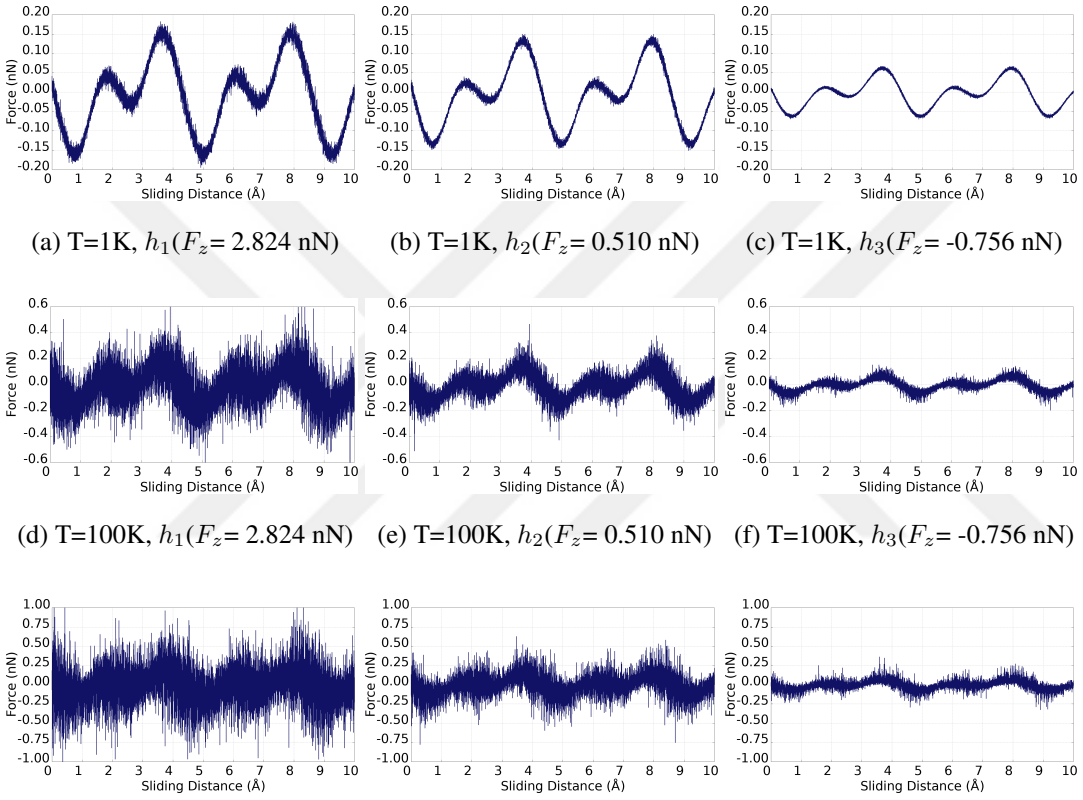

(a) T=1K, $h_1(F_z$= 2.824 nN) (b) T=1K, $h_2(F_z$= 0.510 nN) (c) T=1K, $h_3(F_z$= -0.756 nN)

(d) T=100K, $h_1(F_z$= 2.824 nN) (e) T=100K, $h_2(F_z$= 0.510 nN) (f) T=100K, $h_3(F_z$= -0.756 nN)

(g) T=300K, $h_1(F_z$= 2.824 nN) (h) T=300K, $h_2(F_z$= 0.510 nN) (i) T=300K, $h_3(F_z$= -0.756 nN)

Figure 3.4: Pyramid shape tip sliding along y direction at speed 10 $\frac{cm}{s}$. Y component of the force with respect to distance at different temperatures and loads.

The simulation, in which the lateral force is the most different among all simulations, is created by shifting the pyramid tip in the y direction. The main reasons for this difference is a result of the tip passes exactly over the bond between the graphene atoms and there only being one atom on the contact surface of the tip. In the Figure 3.2, (a)

and (b) can show the exact vertical load during simulation.

3.2.2 Friction Force for Conic Shape Tip

The conical tip serves the purpose of demonstrating the behavior of a tip that is not as sharp as the pyramidal tip but not quite as large as the hemispherical tip (See Figure 3.1). Although more similar to the pyramidal tip in sharpness, the number of atoms in total is smaller. This way, we have the opportunity to observe the contribution of the atoms of the tip that are not in direct contact with the surface.

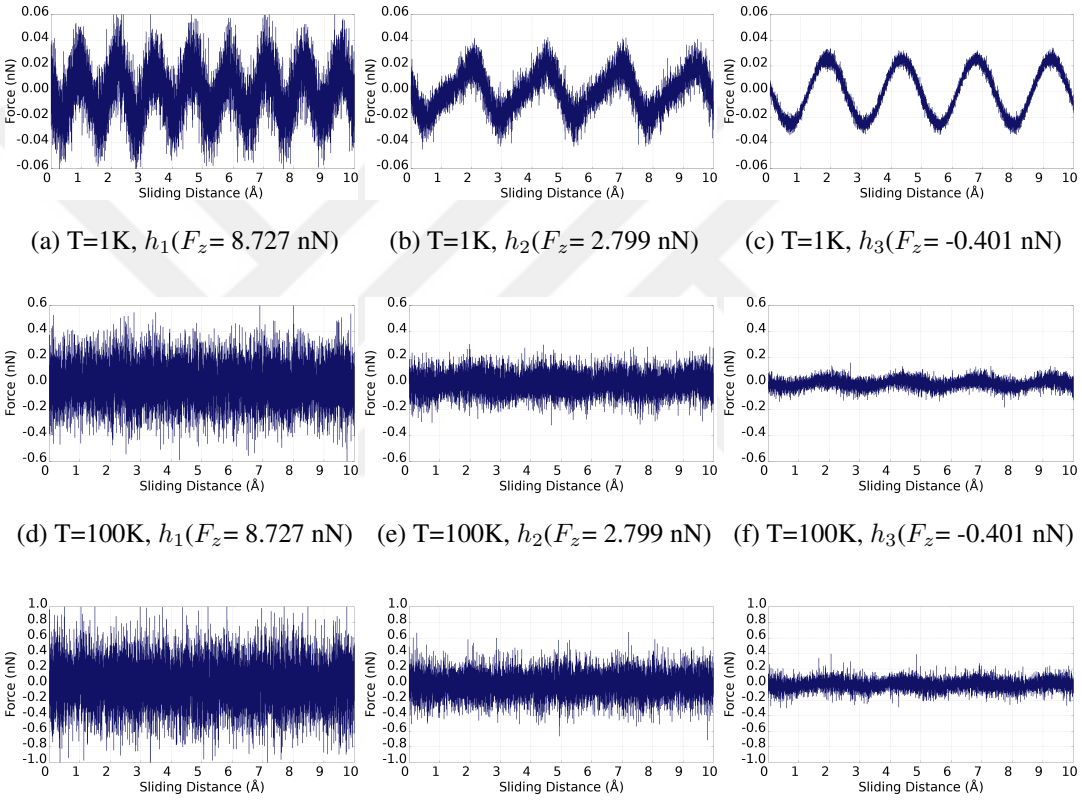

(a) T=1K, $h_1(F_z$= 8.727 nN) (b) T=1K, $h_2(F_z$= 2.799 nN) (c) T=1K, $h_3(F_z$= -0.401 nN)

(d) T=100K, $h_1(F_z$= 8.727 nN) (e) T=100K, $h_2(F_z$= 2.799 nN) (f) T=100K, $h_3(F_z$= -0.401 nN)

(g) T=300K, $h_1(F_z$= 8.727 nN) (h) T=300K, $h_2(F_z$= 2.799 nN) (i) T=300K, $h_3(F_z$= -0.401 nN)

Figure 3.5: Conic shape tip sliding along x direction at speed $10\ \frac{cm}{s}$. X component of the force with respect to distance at different temperatures and loads.

The increase of the surface area, the increase of kinetic energy, and the amount of applied load (can be seen in the Figure 3.2) remained the same throughout the simulation. This causes to not being able to see the zigzag motion directly in the Figure 3.5

at graphs (d), (e), (f), (g), (h), and (i).

It has also been observed that the directional difference can change the friction force. This change may be due to the tendency of the data to perform stick-slip motion in the y direction. This predisposition can be understood from the Figure 3.2.

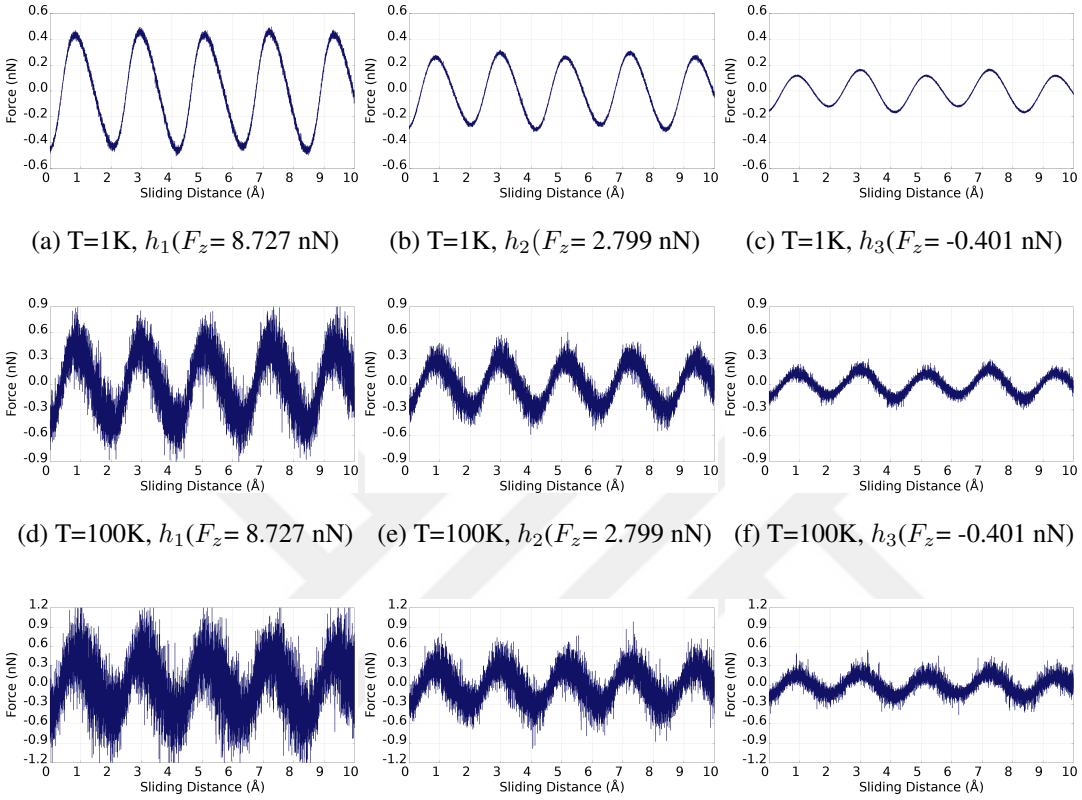

(a) T=1K, $h_1(F_z$= 8.727 nN) (b) T=1K, $h_2(F_z$= 2.799 nN) (c) T=1K, $h_3(F_z$= -0.401 nN)

(d) T=100K, $h_1(F_z$= 8.727 nN) (e) T=100K, $h_2(F_z$= 2.799 nN) (f) T=100K, $h_3(F_z$= -0.401 nN)

(g) T=300K, $h_1(F_z$= 8.727 nN) (h) T=300K, $h_2(F_z$= 2.799 nN) (i) T=300K, $h_3(F_z$= -0.401 nN)

Figure 3.6: Conic shape tip sliding along y direction at speed 10 $\frac{cm}{s}$. Y component of the force with respect to distance at different temperatures and loads.

Interestingly, motion along the y direction restores the periodic behavior at all temperatures, as shown in Figure 3.8. The behavior is once again similar in terms of periodicity but of course with a difference in magnitude for different distances.

3.2.3 Friction Force for Hemisphere Shape Tips

We finish our investigation on the tip shape dependence of friction forces by considering a hemispherical tip. This is the largest tip studied in this section and served to highlight the importance of contact area.

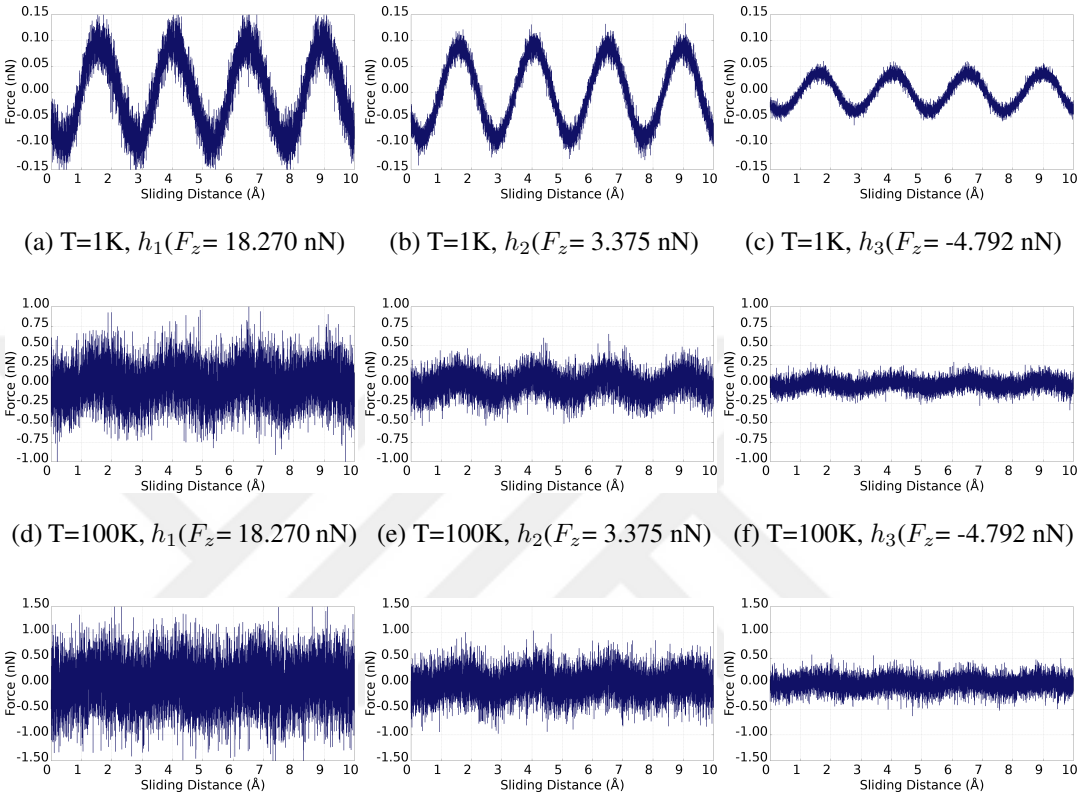

(a) T=1K, $h_1(F_z$= 18.270 nN) (b) T=1K, $h_2(F_z$= 3.375 nN) (c) T=1K, $h_3(F_z$= -4.792 nN)

(d) T=100K, $h_1(F_z$= 18.270 nN) (e) T=100K, $h_2(F_z$= 3.375 nN) (f) T=100K, $h_3(F_z$= -4.792 nN)

(g) T = 300K, $h_1 \equiv$ 18.270 nN (h) T=300K, $h_2(F_z$= 3.375 nN) (i) T=300K, $h_3(F_z$= -4.792 nN)

Figure 3.7: Hemisphere shape tip sliding along x direction at speed $10\ \frac{cm}{s}$. X component of the force with respect to distance at different temperatures and loads.

The sliding along the x direction is surprisingly characterized by the same periodicity as the conical tip, as seen in Figure 3.5. In fact, the overall behavior of these two tips are reminiscent of one another except for the magnitude. As in all cases, the strict periodic structure gives is partially erased by the fluctuations as the temperature increases; however, in contrast to the conical tip, the structure is not entirely lost. The behavior for sliding along the y direction is notably different from all the cases we have observed (See Figure 3.8). The large contact surface brings stronger interactions,

which lead to stick-slip movement in spite of the rigidity of our tips. In Figure 3.8, stick-slip movement can be seen. The reason why this movement seems irregular is that the movement of the gold atoms simulating the AFM tip is restricted. In fact, only contribution to stick-slip movement comes from mobile graphene atoms.

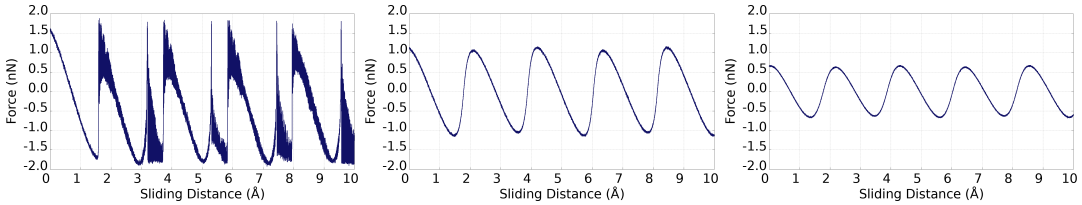

(a) T=1K, h_1(F_z= 18.270 nN) (b) T=1K, h_2(F_z= 3.375 nN) (c) T=1K, h_3(F_z= -4.792 nN)

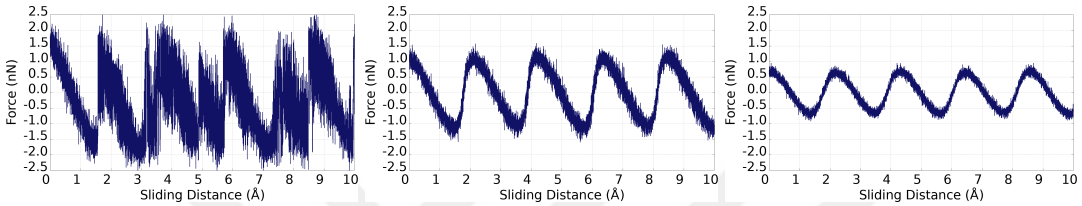

(d) T=100K, h_1(F_z= 18.270 nN) (e) T=100K, h_2(F_z= 3.375 nN) (f) T=100K, h_3(F_z= -4.792 nN)

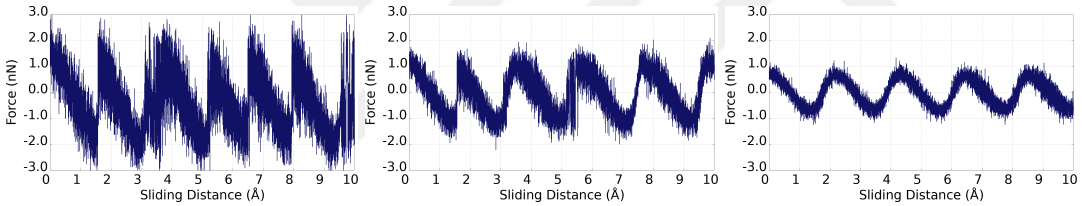

(g) T=300K, h_1(F_z= 18.270 nN) (h) T=300K, h_2(F_z= 3.375 nN) (i) T=300K, h_3(F_z= -4.792 nN)

Figure 3.8: Hemisphere shape tip sliding along y direction at speed 10 $\frac{cm}{s}$. Y component of the force with respect to distance at different temperatures and loads.

During the sliding at 1 Kelvin and h_1 distance, the gold tip adhered to the graphene and caused the graphene to move back and forth during the stick-slip movement. The effect of shaking graphene on lateral force can be seen in the Figure 3.8a.

This concludes our investigation of the details of motion for three different rigid tips. In the next subsection, we compare the friction forces that they experience from a quantitative point of view.

3.3 Comparison of the Three Shapes

The loads applied to the different shaped tips could not be equalized due to the simulation technique used, making it difficult to compare the tip shapes directly. However, a few significant differences emerged. In order to have a clear picture of the differences in the friction force, the tables below have been prepared by taking the average of the forces opposed to the sliding direction of the AFM tip.

Table 3.2: Tips sliding at speed $10\ \frac{cm}{s}$ with respect to different spaces along x and y direction respectively. Average lateral force(nN) at different temperatures and loads.

	Along x direction			Along y direction		
	1K	100K	300K	1K	100K	300K
Pyramid						
h_1 (F_z = 2.824 nN)	0.0960	0.1312	0.1883	0.0811	0.1276	0.1953
h_2 (F_z = 0.510 nN)	0.0824	0.0933	0.1165	0.0646	0.0822	0.1103
h_3 (F_z = -0.756 nN)	0.0384	0.0427	0.0519	0.0303	0.0359	0.0464
Cone						
h_1 (F_z = 8.727 nN)	0.0164	0.1240	0.2246	0.2815	0.3031	0.3537
h_2 (F_z = 2.799 nN)	0.0121	0.0641	0.1175	0.1744	0.1831	0.2085
h_3 (F_z = -0.401 nN)	0.0160	0.0286	0.0509	0.0896	0.0951	0.1079
Hemisphere						
h_1 (F_z = 18.270 nN)	0.0638	0.1979	0.3481	1.1776	1.0498	1.1520
h_2 (F_z = 3.375 nN)	0.0573	0.1179	0.2042	0.6938	0.7159	0.7563
h_3 (F_z = -4.792 nN)	0.0242	0.0597	0.1095	0.4146	0.4277	0.4564

The increase in lateral forces with the rise of temperature and the load is observed in all three systems. This behavior is attributed to the fact that both the large-scale distortions and the collision rates are temperature dependent which can increase the friction force [16].

Although the tips are equidistant to graphene, the force they feel in the vertical di-

rection is different. This is related to the contact surface areas and the number of interacting atoms. On the other hand, different tip shapes directly affect the pressure and deflection of graphene as seen in Table 3.2. This is why, compared to the tables, the pyramid tip feels a larger lateral force during its x direction movement than the other tips. In the sliding along the y direction, passing over the bond reduces the deformation. Due to the high contact surface area and the number of interacting atoms, it is possible to encounter a higher friction force numerically in the sliding process of hemisphere shaped tip as seen in the Table 3.2. Likewise, the widening of the surface area clearly revealed that the friction force during the sliding in the y direction is higher than that in the x direction.

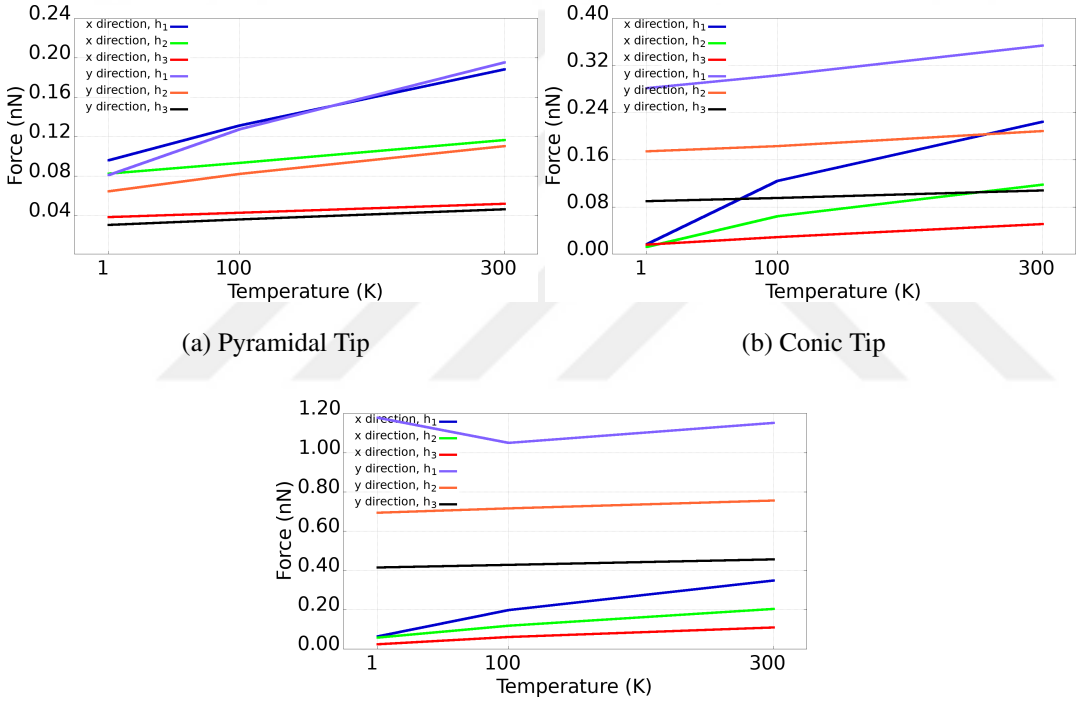

(a) Pyramidal Tip

(b) Conic Tip

(c) Hemispherical Tip

Figure 3.9: Tips sliding at speed 10 $\frac{cm}{s}$ with respect to different spaces along x and y direction respectively. Average friction force with respect to temperatures.

In Figure 3.9, the average friction forces shown in the Table 3.2 are plotted.

It is observed that the vertical force contribution is the only effective parameter for the

pyramidal tip. Unlike the pyramidal tip, the hemispherical tip depends on the direction, and the sliding direction is also effective as well as the vertical load. However, although the direction of the slip has a contribution for a conical tip, it is not sufficient to separate the data. Considering that the sliding direction does not affect the vertical force, the contact surface area is the only remaining change that can affect vertical force with respect to the different sliding direction.

In this section, we presented friction forces experienced by three different rigid tips. This analysis allows us to highlight the importance of shape in the friction problem and isolates the contribution of the substrate in such behavior as stick-slip motion. However, the deformation of the tip is excluded from this discussion. The next section is devoted to the contribution of the tip by means of allowing the lower atoms of the tips to move during the simulations.

CHAPTER 4

INVESTIGATION OF NONRIGID HEMISPHERE GOLD TIPS AND GRAPHENE

In this section, the sliding of the two different sized gold tips along the y axis on the graphene substrate is analyzed in LAMMPS by using MD. The first AFM tip is a nonrigid version of the hemispherical tip used in the previous chapter. The other tip is a hemisphere prepared in huge size compared to the other tips. This calculation includes 77846 atoms during the sliding of the large tip. The thermostat damping parameter and the lateral sliding speed have been increased to 5 fs and 1 $\frac{m}{s}$. Other than this change, the simulation features are the same as the simulations in the previous chapter. In this section, the effects of the rigid and nonrigid tips and sizes of two tips will be examined and compared.

4.1 Determination of Loads on Certain Distances for Smaller Nonrigid Tip

The simulation box used in the simulation of the smaller nonrigid tip is shown in Figure 4.1. The top three layers of the Au tip, as well as the bottom two layers of the multilayer graphene substrate, are kept fixed during the simulations. The multiplayer graphene substrate area was taken to be the same as the rigid system to enable as close a comparison as possible.

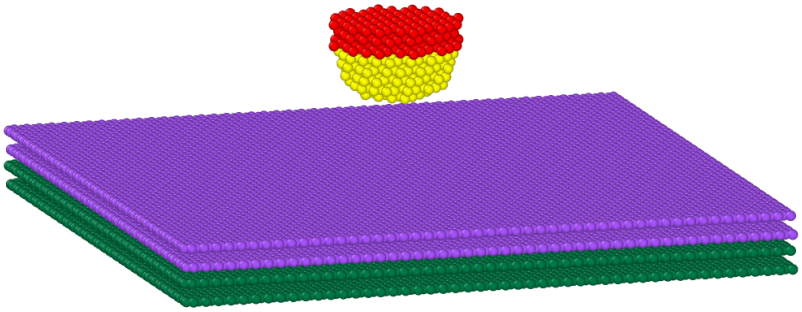

Figure 4.1: Four layered Graphene structure with nonrigid hemisphere gold tip. The bottom green layers and top red gold layers are kept fixed. Area of the multilayer graphene is 14760 $Å^2$.

Due to the way the system was created, as mentioned in the Section 2.6.5 that one may not directly apply load to the system. Therefore similarly to previous simulations, Three different distances between tips and graphene are selected to investigate the effect of AFM tip under loads. These distances are determined based on the distance between the top layer of graphene and the closest atom of the gold tip to this layer. These distances of 0 Å, 0.5 Å and 1 Å are labeled h_4, h_5 and h_6 respectively. However, the distances mentioned here are chosen by assuming that gold will not deform along the z axis. In fact, it should not be expected to maintain the same distance during the simulation. Considering the softness of gold, the selected distances are chosen smaller than the systems with rigid tip.

Loads are calculated by taking the average of the forces on the vertical axis during the sliding processes at room temperature. The vertical force measured as a function of time for the three distances is shown in Figure 4.2.

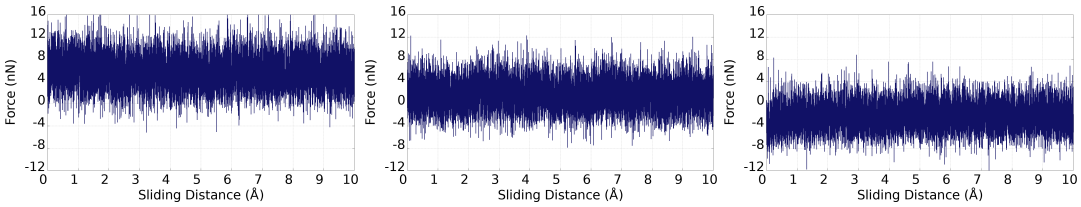

(a) h_4 (b) h_5 (c) h_6

Figure 4.2: Hemisphere shape tip sliding along y direction at 300K temperature and speed 10 $\frac{cm}{s}$. Vertical component of the force with respect to distances.

Due to the softness of the gold AFM tip, the vertical forces are seen to exhibit a constant, as opposed to, oscillatory behavior while at the same time displaying larger fluctuations than the previous results, as seen in the Figure 3.2f. The average vertical forces are listed in Table 4.1.

Table 4.1: Average Loads on hemisphere shape with respect to distances.

Shape	Hemisphere
h_4 (0 Å)	5.780 nN
h_5 (0.5 Å)	1.669 nN
h_6 (1 Å)	-2.299 nN

4.2 Analyzing Friction Force for Nonrigid Tips

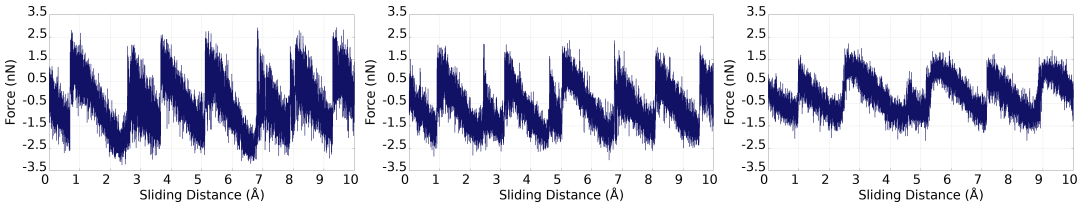

(a) h_4(F_z= 5.780 nN) (b) h_5(F_z= 1.669 nN) (c) h_6(F_z=-2.799 nN)

Figure 4.3: Hemisphere shape tip with mobile atoms sliding along y direction at speed 10 $\frac{cm}{s}$. Y component of the force with respect to distances.

The ability of gold atoms to gain mobility directly shows its resistance to friction force as stick-slip motion. In contrast to the rigid tips, in this case, the stick phase is absorbed by the freer Au atoms, creating an additional source of elasticity. As expected in this system, the friction force increased as the load increased. The reason why the pattern of forces is not the same in the Figure 4.3 on the graphs (a), (b), (c) is the sudden slips of the gold particles. The non-synchronization of the slips can be explained by the sticks which can be variable according to stiffness of the material and load applied during sliding.

Table 4.2: Hemisphere shaped tip sliding at speed 10 $\frac{cm}{s}$ and 300K temperature with respect to different spaces along y direction. Average friction force at different loads.

Hemisphere	Friction Force
h_4 (F_z = 5.780 nN)	1.175 nN
h_5 (F_z = 1.669 nN)	1.086 nN
h_6 (F_z = -2.299 nN)	0.689 nN

4.2.0.1 Comparison of Rigid and Nonrigid Tips

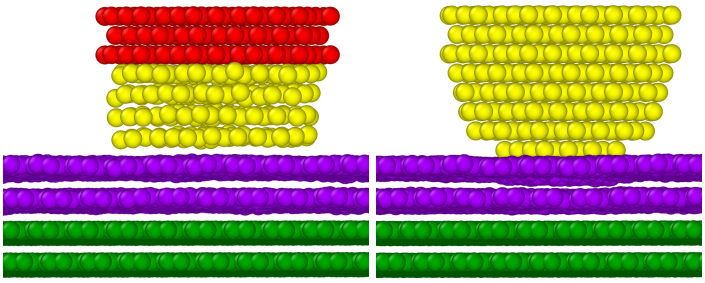

(a) (b)

Figure 4.4: Nonrigid (a) and rigid (b) hemisphere shaped AFM Gold tips respectively. Snapshots are taken during sliding process is ongoing.

The Figure 4.4 shows two gold hemispheres with yellow gold atoms mobile and fixed, top layer distances from the graphene is equal. The response of the two tips is seen

immediately from this figure to be very different from the extra strain introduced by the load. The nonrigid tip absorbs this strain energy by means of completely rearranging the Au atoms to the point of reducing the number of layers by one. The rigid tip, on the other hand, distorts the underlying graphene.

Although there is enough force to push the lower layer to the upper layer, the vertical component of the force which can be seen in the Table 4.3 is negative after the gold atoms stabilize in the upper layer. This comparison shows that the material used as the tip will directly affect the measurements. The tips that are pressed enough to create bending in the graphene causes the graphene to gather in front of the tip and react more during sliding, which causes the friction force to increase considerably [56].

Table 4.3: Hemisphere shaped tips sliding along y direction at speed $10\ \frac{cm}{s}$ and 300K temperature. Average friction forces and loads.

Hemisphere	NonRigid	Rigid
Load	-2.299 nN	18.270 nN
Friction Force	0.689 nN	1.152 nN
Distance	h_6 = 1 Å	h_1 = 2 Å

4.3 Indentation Analysis

In this section, the AFM tip is progressively pressed into the 6-layer graphene similar to indentation experiments to analyze the massive load difference observed during the comparison of the two hemispheres in Section 4.2.0.1. In the calculations presented in this section, we model the substrate with a 6-layer graphene sample instead of the previous 4-layer model to not over-constrain any elastic response. In fact, our results show that the elastic response goes as far as the third layer. In the Figure 4.5, it is possible to see directly that the pressure on the graphene both decreased and increased even though the tip moved vertically to the graphene.

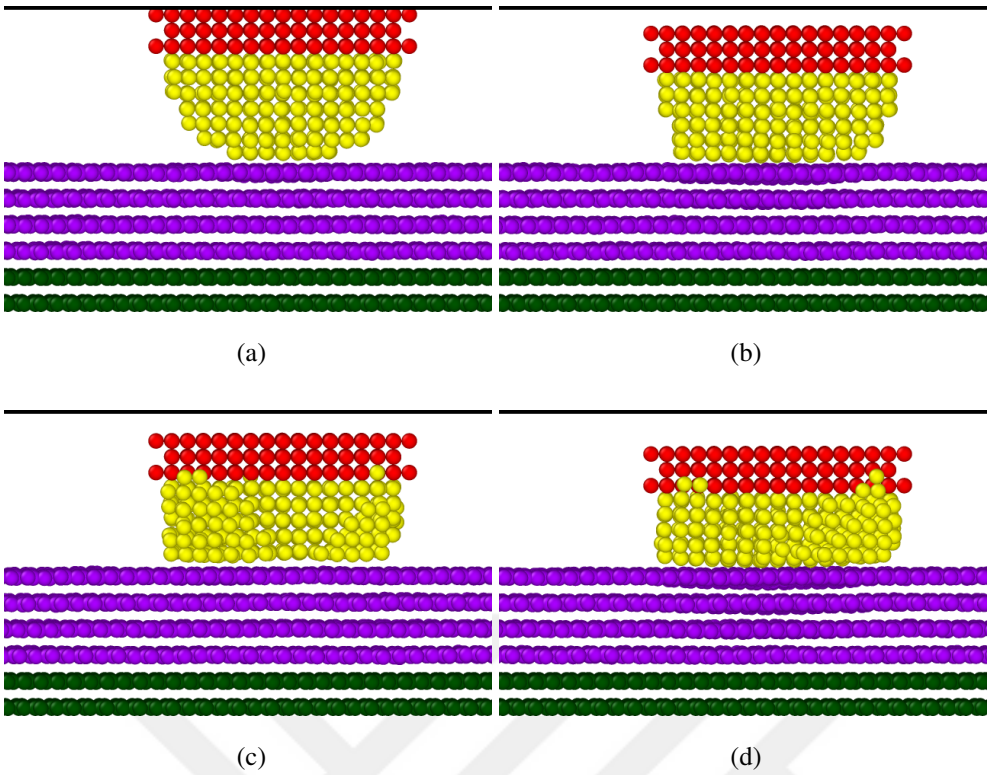

Figure 4.5: Starting from (a), in each graph hemisphere tip moves along -z direction.

During the vertical displacement of the tip for a total of 3.5 Å, a mixture of deformation of the tip and the bending of the graphene substrate can be seen. The mean square displacement (MSD) of the mobile graphene layers has been plotted along the movement of the tip in the Figure 4.6 to better understand the response during this movement. The tip crushing due to the softness of the gold directly affected the MSD. There is a sudden drop in vertical force at the time the crushing occurred, and it is the first layer of graphene that is most affected.

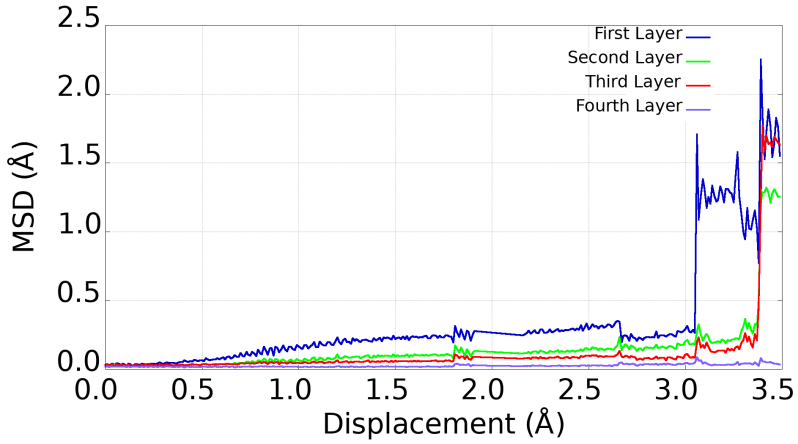

Figure 4.6: Change in the MSD of mobile graphene layers while tip moves along -z direction.

The ease with which the Au atoms in the tip are displayed clearly affects the frictional forces. In the next section, we analyze the extent to which this property scales up to larger sizes.

4.4 Enormous Tip

To examine the contribution of the AFM tip's size to the measurement, the golden hemisphere seen in the Figure 4.7 is created. In order to reduce the computational cost, the frequency of activation of the thermostat is increased to 5 fs, and the tip speed during sliding is increased to 1 $\frac{m}{s}$. It is predicted that these changes would not affect the measurements since the system is large enough to stabilize sudden changes. To reduce the cost, a single load is chosen for sliding once, enough not to distribute the structure of the AFM tip.

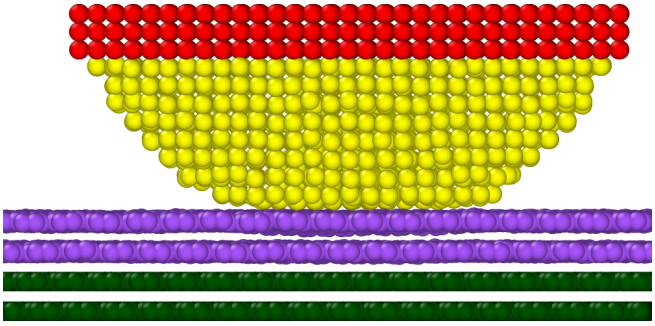

Figure 4.7: 4 layered Graphene with enormous hemisphere gold tip.

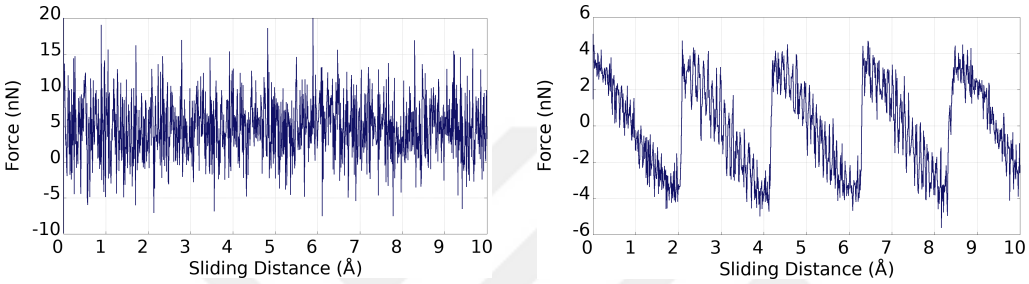

(a) Vertical Force

(b) Lateral Force

Figure 4.8: Enormous tip sliding at speed 1 $\frac{m}{s}$ and 300 K temperature. Average load and friction force.

As seen in the Figure 4.8a, the gold tip continued to slide under a constant load. It is expected that this is the simulation in which the effects of the stick-slip movement are most apparent due to the size of the type. This motion indicates that the friction is static.

Table 4.4: Average load and friction force.

Load	4.922 nN
Friction Force	2.213 nN

As predicted, the distortion of the Au tip at this size is much small, and the strain energy is absorbed by distorting the graphene substrate. Of course, this doesn't exclude smaller elastic distortions of the tip. Therefore the response is likely a combination

of both. In any case, we reach the critical result that to obtain a stick-slip reaction at elevated temperatures, one needs a large enough tip.

CHAPTER 5

CONCLUSION

In this thesis, we investigated the nanotribological properties between gold and industrially important graphene. The gold atoms are formed in types to simulate the AFM tip, while graphene was created as a substrate. The motivation behind this work stems from the great interest in graphene being used as a lubricant and reinforcement material. Since graphene has remarkable mechanical properties, it is used very often for these purposes. Our main aim here was to understand the interaction between graphene and gold, the effect of macroscopic properties of the AFM type on measurements, and provide input for their development.

In Chapter 3, the vertical component of the forces of the different rigid tips with graphene are calculated to observe the stress on the graphene. Then, the tips with different temperatures, loads, and shapes were shifted at a constant speed in both x and y directions. Since the movement of gold atoms is limited, the vertical component of the forces in this chapter are high and have created bending on graphene. When the loads in both directions are examined, it has been observed that the patterns of the vertical component of the forces are shaped by the carbon-carbon bonds in the graphene. In fact, the average load is the same for both the sliding process, but its fluctuations are different. The lateral forces are affected by temperature, load, and shape, as well as the direction of the sliding. The increase in load and temperature directly affected the lateral forces as become higher. Different shapes of the tips have shown us the importance of the contact point while measuring the lateral force. For example: When examining the sliding in the y direction in the pyramid shaped AFM simulation, the lateral force of the tip has clearly changed as it passes over the bonds. Apart from these, the friction force is higher in the y direction sliding operations

than in the x direction. In the simulations in this chapter, the effects of the stick-slip movement on the sliding process that takes place parallel to the bonds have been observed slightly.

In Chapter 4, the only hemisphere is chosen as the form of AFM. A hemisphere of the size used in the previous chapter and a hemisphere with very large size are used in simulations. In contrast to the previous chapter, the movement of gold material at the AFM tip used is not restricted. First, the small radius hemisphere is shifted at different loads along y direction at 300K. Then, the enormous AFM tip was shifted under the same conditions. Our aim in this chapter is to reveal the difference in the use of hard and soft materials in AFM tips and to test whether the tip sizes used in simulations are realistic. For this, the small hemisphere used in this chapter, and the one from the previous chapter has been compared. When soft material is used, it has been observed that the vertical forces of the AFM tips change when they are crushed under pressure. To analyze this change in more detail, gold tip is pushed into six layer graphene. The crushing of the layers of gold prevents the graphene from bending by suddenly reducing the vertical pressure. It has been stated in the literature that the bending of graphene under type pressure will increase the lateral force during sliding. Following this analysis, the sliding process was simulated with the enormous AFM tip. The stick-slip movement encountered while examining the lateral force indicates that the friction is static.

In future studies, phonon modes during sliding can be measured under the pressure of the AFM tip; the heat map caused by friction and how this energy is distributed can be investigated; the buckling effect [57] that will occur as a result of shifting with a large nonrigid AFM tip can be researched with single-layer graphene that may be used as a coating. Also, friction studies between these two materials could be taken a step further using DFT. Since we used many-body potentials, we did not have the opportunity to examine the electrical properties. This situation is not a restriction to DFT research. The dielectric constant of graphene can be examined as gold and graphene approach each other.

REFERENCES

[1] A. H. Castro Neto, F. Guinea, N. M. R. Peres, K. S. Novoselov, and A. K. Geim, "The electronic properties of graphene," *Rev. Mod. Phys.*, vol. 81, pp. 109–162, Jan 2009.

[2] Y. Song and B. Bhushan, "Atomic force microscopy dynamic modes: Modeling and applications," *Journal of Physics: Condensed Matter*, vol. 20, p. 225012, 05 2008.

[3] G. B. D. of Education and Science, *Lubrication (tribology), education and research: a report on the present position and industry's needs*. H. M. Stationery Off., 1966.

[4] K. Holmberg and A. Erdemir, "Influence of tribology on global energy consumption, costs and emissions," *Friction*, vol. 5, pp. 263–284, 09 2017.

[5] L. Murr, *Computer Simulation in Materials Science and Engineering*, pp. 1105–1121. 01 2015.

[6] X. Li and L. Zhi, "Graphene hybridization for energy storage applications," *Chemical Society Reviews*, vol. 47, 03 2018.

[7] J. Puértolas and S. Kurtz, "Evaluation of carbon nanotubes and graphene as reinforcements for uhmwpe-based composites in arthoplastic applications: A review," *Journal of the Mechanical Behavior of Biomedical Materials*, vol. 39, pp. 129–145, 06 2014.

[8] R. Young, M. Liu, I. Kinloch, S. Li, X. Zhao, C. Vallés, and D. Papageorgiou, "The mechanics of reinforcement of polymers by graphene nanoplatelets," *Composites Science and Technology*, vol. 154, 11 2017.

[9] Y. Liu, B. Xie, Z. Zhang, Q. Zheng, and Z. Xu, "Mechanical properties of graphene papers," *Journal of the Mechanics and Physics of Solids*, vol. 60, 04 2011.

[10] J. Liu, J. Notbohm, R. Carpick, and K. Turner, "Method for characterizing nanoscale wear of atomic force microscope tips," *ACS nano*, vol. 4, pp. 3763–72, 07 2010.

[11] G. T. B.Sc., "Cvi. a molecular theory of friction," *The London, Edinburgh, and Dublin Philosophical Magazine and Journal of Science*, vol. 7, no. 46, pp. 905–939, 1929.

[12] V. Popov and J. Gray, *Prandtl-Tomlinson Model: A Simple Model Which Made History*, pp. 153–168. 01 2014.

[13] V. Perfilyev, A. Moshkovich, I. Lapsker, A. Laikhtman, and L. Rapoport, "Dislocation structure and stick–slip phenomenon," *Tribology Letters*, vol. 55, 08 2014.

[14] S. Qiao and Q. Li, "Sliding friction and contact angle hysteresis of droplets on microhole-structured surfaces," *The European Physical Journal E*, vol. 41, 02 2018.

[15] E.-S. Yoon, A. Singh, H.-J. Oh, and H. Kong, "The effect of contact area on nano/micro-scale friction," *Wear*, vol. 259, pp. 1424–1431, 07 2005.

[16] P. He, Q. Cao, P. Wang, H. Wang, S. Zheng, S. Lei, S. Liu, and Q. Peng, "Grain boundary regulates friction behaviors between graphene and gold substrate," *Crystals*, vol. 9, p. 418, 08 2019.

[17] N. John and G. Kulkarni, "Gold-coated conducting-atomic force microscopy probes," *Journal of nanoscience and nanotechnology*, vol. 5, pp. 587–91, 05 2005.

[18] D. Berman, A. Erdemir, and A. V. Sumant, "Graphene: a new emerging lubricant," *Materials Today*, vol. 17, no. 1, pp. 31 – 42, 2014.

[19] Y. Park, J. Koo, S. Kim, and H. C. Choi, "Spontaneous formation of gold nanoparticles on graphene by galvanic reaction through graphene," *ACS Omega*, vol. 2019, 10 2019.

[20] M. Lodge, C. Tang, B. Blue, W. Hubbard, A. Martini, B. Dawson, and

M. Ishigami, “Lubricity of gold nanocrystals on graphene measured using quartz crystal microbalance,” *Scientific Reports*, vol. 6, p. 31837, 08 2016.

[21] T. Oznuluer Ozer, E. Pinçe, E. Polat, O. Balci, O. Salihoglu, and C. Kocabas, “Synthesis of graphene on gold,” *Applied Physics Letters - APPL PHYS LETT*, vol. 98, 03 2011.

[22] P. Zhu and R. Li, “Study of nanoscale friction behaviors of graphene on gold substrates using molecular dynamics,” *Nanoscale Research Letters*, vol. 13, 12 2018.

[23] S. Plimpton, “Journal of computational physics, vol 117, p 1–19 (1 march 1995) fast parallel algorithms for short–range molecular dynamics,” *J. Comput. Phys.*, vol. 117, 08 2000.

[24] L. Verlet, “Computer "experiments" on classical fluids. i. thermodynamical properties of lennard-jones molecules,” *Phys. Rev.*, vol. 159, pp. 98–103, Jul 1967.

[25] W. C. Swope, H. C. Andersen, P. H. Berens, and K. R. Wilson, “A computer simulation method for the calculation of equilibrium constants for the formation of physical clusters of molecules: Application to small water clusters,” *The Journal of Chemical Physics*, vol. 76, no. 1, pp. 637–649, 1982.

[26] P. Schofield, “Computer simulation studies of the liquid state,” *Computer Physics Communications*, vol. 5, no. 1, pp. 17 – 23, 1973.

[27] S. Carnot and R. Fox, *Reflexions on the Motive Power of Fire: A Critical Edition with the Surviving Scientific Manuscripts*. Manchester University Press, 1986.

[28] J. Cai and Y. Ye, “Simple analytical embedded-atom-potential model including a long-range force for fcc metal and their alloys,” *Physical review. B, Condensed matter*, vol. 54, pp. 8398–8410, 10 1996.

[29] J. E. Jones and S. Chapman, “On the determination of molecular fields ii. from the equation of state of a gas,” *Proceedings of the Royal Society of London. Series A, Containing Papers of a Mathematical and Physical Character*, vol. 106, no. 738, pp. 463–477, 1924.

[30] R. Costa Filho, G. Alencar, B.-S. Skagerstam, and J. Jr, "Morse potential derived from first principles," *EPL (Europhysics Letters)*, vol. 101, p. 10009, 01 2013.

[31] S. J. Stuart, A. B. Tutein, and J. A. Harrison, "A reactive potential for hydrocarbons with intermolecular interactions," *The Journal of Chemical Physics*, vol. 112, no. 14, pp. 6472–6486, 2000.

[32] H.-J. Butt and M. Kappl, *van der Waals Forces*, pp. 43–98. 04 2018.

[33] J. Rackers and J. Ponder, "Classical pauli repulsion: An anisotropic, atomic multipole model," *The Journal of Chemical Physics*, vol. 150, p. 084104, 02 2019.

[34] M. Neek-Amal, R. Asgari, and M. R. R. Tabar, "The formation of atomic nanoclusters on graphene sheets," *Nanotechnology*, vol. 20, p. 135602, mar 2009.

[35] M. S. Daw and M. I. Baskes, "Embedded-atom method: Derivation and application to impurities, surfaces, and other defects in metals," *Phys. Rev. B*, vol. 29, pp. 6443–6453, Jun 1984.

[36] D. Brenner, O. Shenderova, J. Harrison, S. Stuart, B. Ni, and S. Sinnott, "A second-generation reactive empirical bond order (rebo) potential energy expression for hydrocarbons," *J. Phys.: Condens. Matter*, vol. 14, pp. 783–802, 02 2002.

[37] D. Frenkel and B. Smit, *Understanding molecular simulation : from algorithms to applications. 2nd ed*, vol. 50. 01 1996.

[38] J. Hickman and Y. Mishin, "Temperature fluctuations in canonical systems: Insights from molecular dynamics simulations," *Physical Review B*, vol. 94, 09 2016.

[39] S. Nose, "A molecular dynamics method for simulations in the canonical ensemble," *Mol. Phys.*, vol. 100, pp. 191–198, 01 2002.

[40] H. Eslami, "Molecular dynamics simulation in the grand canonical ensemble," *Journal of computational chemistry*, vol. 28, 07 2007.

[41] H. C. Andersen, "Molecular dynamics simulations at constant pressure and/or temperature," *The Journal of Chemical Physics*, vol. 72, no. 4, pp. 2384–2393, 1980.

[42] W. G. Hoover and B. L. Holian, "Kinetic moments method for the canonical ensemble distribution," *Physics Letters A*, vol. 211, pp. 253–257, Feb. 1996.

[43] R. L. Davidchack, R. Handel, and M. V. Tretyakov, "Langevin thermostat for rigid body dynamics," *The Journal of Chemical Physics*, vol. 130, no. 23, p. 234101, 2009.

[44] H. J. C. Berendsen, J. P. M. Postma, W. F. van Gunsteren, A. DiNola, and J. R. Haak, "Molecular dynamics with coupling to an external bath," *The Journal of Chemical Physics*, vol. 81, no. 8, pp. 3684–3690, 1984.

[45] S. Kim, "Issues on the choice of a proper time step in molecular dynamics," *Physics Procedia*, vol. 53, p. 60–62, 12 2014.

[46] Y. Dong, Q. Li, and A. Martini, "Molecular dynamics simulation of atomic friction: A review and guide," *Journal of Vacuum Science & Technology A: Vacuum, Surfaces, and Films*, vol. 31, pp. 030801–030801, 05 2013.

[47] R. Promyoo, H. Elmounayri, and K. Varahramyan, "Molecular dynamics simulation model of afm-based nanomachining," *Computer Science & Information Technology*, vol. 4, 11 2014.

[48] Y. Hasegawa and P. Avouris, "Manipulation of the reconstruction of the au(111) surface with the stm," *Science (New York, N.Y.)*, vol. 258, pp. 1763–5, 01 1993.

[49] E. Braun, S. M. Moosvai, and B. Smit, "Anomalous effects of velocity rescaling algorithms: The flying ice cube effect revisited," *Journal of Chemical Theory and Computation*, vol. 14, 08 2018.

[50] H. A. Lorentz, "Ueber die anwendung des satzes vom virial in der kinetischen theorie der gase," *Annalen der Physik*, vol. 248, no. 1, pp. 127–136, 1881.

[51] M. Waldman and A. Hagler, "New combining rules for rare gas van der waals parameters," *Journal of Computational Chemistry*, vol. 14, no. 9, pp. 1077–1084, 1993.

[52] B. E. F. Fender and G. D. Halsey, "Second virial coefficients of argon, krypton, and argon-krypton mixtures at low temperatures," *The Journal of Chemical Physics*, vol. 36, no. 7, pp. 1881–1888, 1962.

[53] C. L. Kong, "Combining rules for intermolecular potential parameters. ii. rules for the lennard-jones (12–6) potential and the morse potential," *The Journal of Chemical Physics*, vol. 59, no. 5, pp. 2464–2467, 1973.

[54] W. Pauli, "Über den Zusammenhang des Abschlusses der Elektronengruppen im Atom mit der Komplexstruktur der Spektren," *Zeitschrift fur Physik*, vol. 31, pp. 765–783, Feb. 1925.

[55] D. Berman, A. Erdemir, and A. Sumant, "Approaches for achieving superlubricity in two-dimensional materials," *ACS Nano*, vol. 12, 03 2018.

[56] Y. Dong, X. Wu, and A. Martini, "Atomic roughness enhanced friction on hydrogenated graphene," *Nanotechnology*, vol. 24, p. 375701, 08 2013.

[57] A. Kleinbichler, M. Pfeifenberger, J. Zechner, S. Wöhlert, and M. Cordill, "Scratch induced thin film buckling for quantitative adhesion measurements," *Materials & Design*, vol. 155, 05 2018.